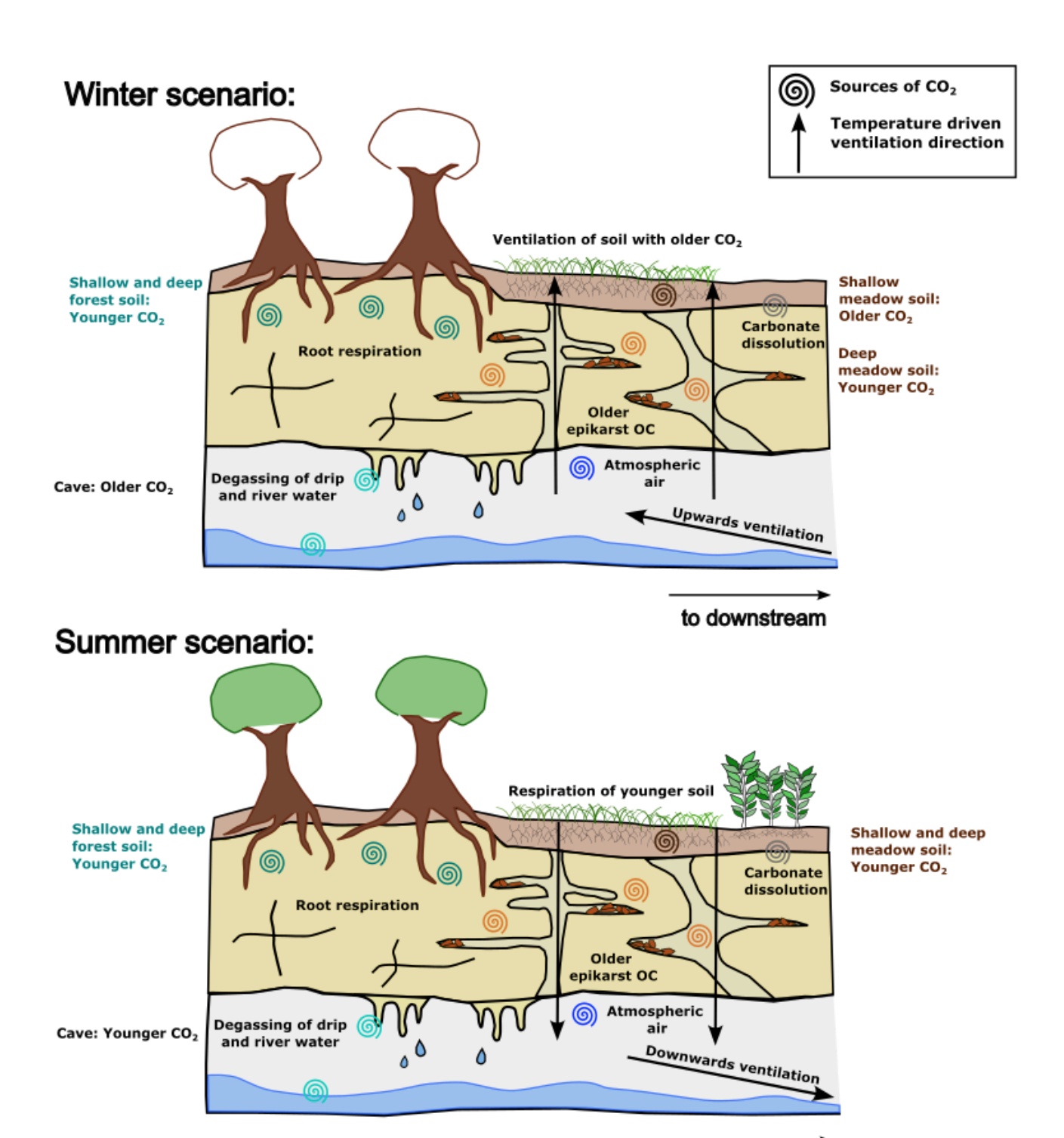
1 Subsurface CO₂ dynamics in a temperate karst system reveal 2 complex seasonal and spatial variations

4 Sarah Rowan^{1,2}, Marc Luetscher³, Thomas Laemmel^{1,2}, Anna Harrison⁴, Sönke Szidat^{1,2}, Franziska A 5 Lechleitner^{1,2}

- 7 Department of Chemistry, Biochemistry, and Pharmaceutical Sciences, University of Bern, 3012, Bern, Switzerland.
- 8 ²Oeschger Centre for Climate Change Research (OCCR), University of Bern, 3012, Bern, Switzerland
- 9 ³ Swiss Institute of Speleology and Karst Studies, 2300, La Chaux-de-Fonds, Switzerland.
- 10 ⁴ Institute of Geological Sciences, University of Bern, 3012, Bern, Switzerland.
- 11 Correspondence to: Sarah Rowan (sarahrowan96gmail.com)

12 Abstract. Understanding the carbon cycle of the terrestrial Critical Zone, extending from the tree canopy to the aquifer, is 13 crucial for accurate quantification of its total carbon storage and for modelling terrestrial carbon stock responses to climate 14 change. Caves and their catchments offer a natural framework to sample and analyse carbon in unsaturated zone reservoirs 15 across various spatial and temporal scales. In this study, we analyse the concentration, stable carbon isotopic ratio (δ^{13} C), and 16 radiocarbon (14C) compositions of CO₂ from the atmosphere, boreholes (0.5 to 5 m depth), and cave sampled every two 17 months over two years at Milandre cave in northern Switzerland. High concentrations of up to 35,000 ppmV CO₂ are 18 measured in the boreholes. The δ^{13} C values of CO₂ in the boreholes reflect the δ^{13} C of C3 plants (~ -26 ‰) which dominate 19 the catchment ecosystem. Shallow meadow boreholes host older CO₂ in winter and modern CO₂ in summer, while forest 20 ecosystems consistently export modern CO_2 ($F^{14}C = \sim 1$) to the unsaturated zone. Cave CO_2 concentrations exceed 21 atmospheric levels and are diluted by temperature-driven seasonal ventilation. Keeling plot intercepts indicate that the cave 22 CO₂, which mixes with atmospheric CO₂, is younger in summer (F¹⁴C = 0.94) and older in winter (F¹⁴C = 0.88), with a δ ¹³C 23 consistent with the C3 plant dominated catchment. Mixing models utilising drip water dissolved inorganic carbon ¹⁴C 24 suggest that varying carbonate dissolution and degassing dynamics do not explain the $F^{14}C$ variation and concurrent $\delta^{13}C$ 25 stability of the mixing endmember. Rather, contributions from aged carbon reservoirs in the deeper unsaturated zone are 26 likely. This study provides valuable insights into CO₂ source dynamics and cycling within the karstic Critical Zone, 27 highlighting the impact of seasonal variations and ecological factors on downward carbon export from terrestrial ecosystems. 28



to downstream

30 1 Introduction

Within the context of current and future climate change, investigations into the response of Critical Zone carbon pools to 32 rising temperatures and changing hydroclimatic conditions are crucial (Brantley et al., 2007). Recent studies have 33 specifically highlighted the unsaturated zone as a potentially important but poorly constrained reservoir of gaseous CO₂ 34 (Mattey et al., 2016; Noronha et al., 2015; Keller, 2019; Stewart et al., 2022). Estimates suggest that between 2 to 53 PgC 35 could be present in the form of CO₂ in the unsaturated zone globally (Baldini et al., 2018). This carbon is particularly 36 vulnerable to changes in the water table level, whereby rises may easily result in the rapid release of CO₂ into the atmosphere 37 (Baldini et al., 2018). Despite its importance, comprehensive assessments integrating spatial and temporal variability of 38 shallow subsurface CO₂ remain scarce.

39

40 Understanding unsaturated zone CO₂ dynamics is complicated by the different sources of carbon contributing to the 41 subsurface reservoir. The CO₂ present in the unsaturated zone is often referred to as ground air and was first defined as CO₂ 42 produced by microbial oxidation of organic material which was transported from the surface (Atkinson, 1977). However, 43 ground air can also refer more generally to high CO₂ concentrations in the subsurface, without linking its presence to a 44 particular source. Early evidence for the presence of a ground air reservoir was the observation of high CO₂ concentrations 45 found in deep cave passages with poor connection to the catchment surface, suggesting an endogenous source of CO₂ 46 (McDonough et al., 2016). The age profile of this high concentration CO₂ reservoir, however, varies by site, suggesting 47 significant variability in its source and processing. CO₂ reservoirs of a lower F¹⁴C, corresponding to an older age, have been 48 reported (Breecker et al., 2012; Noroha et al., 2015; Mattey et al., 2016; Bergel et al., 2017), as well as modern subsurface 49 CO₂ pools, likely derived from ecosystem respiration of recently fixed carbon (Campeau et al., 2019; Tune et al., 2020). 50 Consequently, the primary sources of subsurface CO₂ generally considered are 1) the outside atmosphere (Kukuljan et al., 51 2021), 2) catchment soil and vegetation respiration (Breecker et al., 2012; Li et al., 2024), 3) microbial respiration in the 52 unsaturated zone (Mattey et al., 2016; Ravn et al., 2020), 4) carbon dissolved from the carbonate bedrock (Milanolo & 53 Gabrovšek, 2015), and 6) volcanic and metamorphic hydrothermal input (Chiodini et al., 2008; Girault et al., 2018).

54

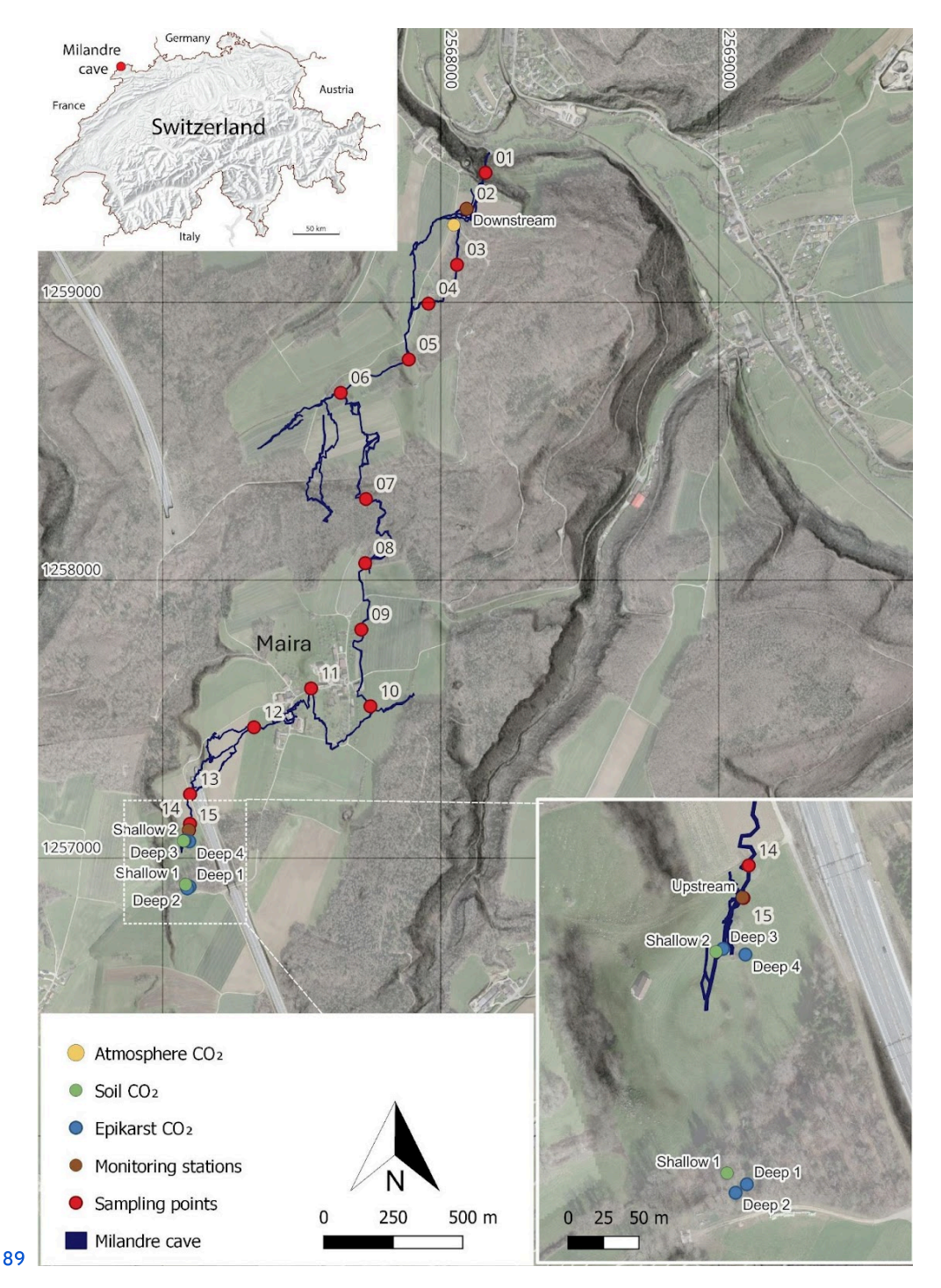
55 Carbon isotope analysis of CO₂ can be used to differentiate the contributing sources to the subsurface gas mixture. 56 Specifically, the δ¹³C of CO₂ in the unsaturated zone can provide information about the influence of biological fractionation 57 by overlying catchment vegetation and microbial respiration, and the influence of carbonate dissolution and subsequent 58 degassing (Breecker et al., 2017, McDonough et al., 2016). In addition, due to the contrast between the ¹⁴C content of 59 biospheric carbon, which ranges from bomb peak enriched to >10,000 years old, and carbonate rock which is typically 60 radiocarbon dead, ¹⁴C measurements of subsurface CO₂ can provide information for both source apportionment and carbon 61 turnover rates in the terrestrial subsurface (Noronha et al., 2015).

63 Though there has been extensive work investigating unsaturated zone CO_2 reservoirs, questions remain about the 64 concentration, composition and sources of ground air on temporal and spatial scales. This study seeks to address this gap by 65 presenting a detailed assessment of CO_2 concentrations and isotopic compositions over 2 years within the Milandre cave 66 karst system in Switzerland. We aim to 1) Determine the relationships between pCO_2 , $\delta^{13}CO_2$, and $^{14}CO_2$ in Milandre cave 67 and its catchment; 2) Assess the effect of seasonality on CO_2 concentration and isotopic characteristics and 3) Gain insights 68 into the provenance of CO_2 and how these evolve over time.

69 2 Site Overview

88

70 Milandre cave (47.4852 ° N, 7.0161 ° E, 373m a.s.l.) is located in the municipality of Boncourt in the Jura canton, NW 71 Switzerland (Fig. 1). The Milandre karst structure formed within the Jura mountains, a sub-alpine mountain range which lies 72 laterally in a northwest-southeast direction. The cave is located within the external Plateau unit of the Jura mountains which 73 consists of thin sub horizontal Mesozoic limestone units that have experienced deformation which produced imbricates and 74 strike-slip faults (Sommaruga, 2011). More specifically, the Milandre karst system formed within the Late Jurassic (Middle 75 Oxfordian) St-Ursanne Formation which overlies Early to Middle Oxfordian marls (Jeannin, 1998). The unsaturated zone 76 ranges between 40 and 80 m depth. The active karst level developed in the epiphreatic zone, with the underneath phreatic 77 zone extending for ~ 20 m to reach the low permeable Lower Oxfordian marls (Liesberg Mb) (Perrin et al., 2003). The cave 78 is formed over 2.7 km, with 10.5 km of galleries forming along N-S oriented fractures. The Milandre river flows for 4.5 km 79 in a northerly direction in the lower part of the cave and exits via the perennial Saivu spring where it joins the Allaine River, 80 and the Bame temporary spring. Clays and silts, deposited during hydraulic backflooding, are particularly present in the 81 downstream part of Milandre cave where they contribute to the sediment load during mild flood events. In contrast, during 82 medium to intense flow, allochthonous sediment transport is often associated with higher microbial concentrations 83 (Vuilleumier et al., 2021). Quantifying the contribution of microbial respiration to the cave carbon cycle was beyond the 84 scope of this study and should be addressed by future research. The Milandre river drains a catchment area of approximately 85 13 km² (Perrin et al., 2003). There is a series of dolines in the catchment area which form depressions ~10 to 20 m deep in 86 the landscape. Notably, one doline is located in the meadow partially covering the upstream section of Milandre cave (Fig. 87 1).



90 Figure 1. Map of the main passages of the Milandre cave network. The location of the atmospheric sampling (yellow), the soil 91 (green) and unsaturated zone boreholes (blue), and the cross-trip sampling (red) are annotated. Cave survey modified from Gigon

92 & Wenger (1986). Base map from ©swisstopo.

93 Over the past 40 years, land use in the catchment area has been dominated by farmland (37 %), forest (36 %), and meadows 94 (12 %) as estimated by aerial photo analysis (Jeannin et al., 2016). The crops grown primarily include maize and tobacco, 95 two C4 plants. Long-term land use analysis shows that farmland has decreased slightly in this area and special infrastructures 96 have increased due to the construction of a motorway that overlies part of the cave. The soils of the area are influenced by 97 the ecosystem that is overlying it. Forest soils are shallow leptosols (< 10 cm deep) that are rich in fragments of the 98 carbonate bedrock. The shallow forest soils transition into deeper (up to ~ 80 cm) organic rich histosols in the meadows, 99 particularly in the dolines. The roots from the forest vegetation likely extend into the epikarst and unsaturated zone, however 100 no roots are visible within the cave itself.

101

The Jura region experiences a marine west coast, warm summer climate (Cfb classification) (Kottek et al., 2006). Daily temperature measurements from the Fahy MeteoSwiss weather station located ~ 9.5 km SW from Milandre cave show a 104 mean temperature of 9.4 °C (1991 to 2020). Temperature seasonality is strong, with monthly mean temperatures fluctuating 105 between a minimum of -1.2 °C in January and a maximum of 18.2 °C in July from 1991 to 2020 (MeteoSwiss, 2024). In 106 contrast, temperatures within the cave remain almost constant year-round, and vary between 10.3 and 11.0 °C (Affolter et al., 107 2020). The temperature difference between the outside and in-cave temperature drives dynamic ventilation on seasonal 108 scales (Garagnon et al., 2022). Regional meteoric precipitation shows a mean of 1,046 mm year-1. Monthly precipitation data 109 indicate that precipitation in this area is well dispersed throughout the year (MeteoSwiss, 2024). Monitoring of tritium (³H) 110 in stalagmite drip water was used to estimate the residence time of seepage water at ~ 5.5 to 6.6 years (Affolter et al., 2020).

111 3 Materials and methods

112 3.1 Gas sampling set up

113 All gas samples were taken every two months from December 2021 to January 2024. The samples were collected in 5 L 114 sampling bags (Cali-5-Bond, Calibrated Instruments, USA) using a handheld pump. The gas was dried through a glass tube 115 filled with granular magnesium perchlorate (~ 83 % purity, Supelco, Germany) to reduce the effects of humidity which may 116 affect the isotopic composition of the sample. The sampling set up and procedure were identical for all gas samples. The CO₂ 117 concentration was monitored during line flushing using a nondispersive infrared (NDIR) CO₂ sensor (SCD30, Sensirion, 118 Switzerland) to ensure accurate sampling. The magnesium perchlorate was exchanged before each sampling day. Prior to 119 analysis, the samples were stored away from direct sunlight in cool indoor temperatures for a maximum of six weeks. The 120 same bags were reused for each sampling location and were flushed with N₂ gas for at least 48 h before sampling to reduce 121 cross contamination risks.

123 Atmospheric samples were collected at a defined sampling site above the cave (Fig. 1). Before sampling, the line was 124 manually flushed for 1 min. To reduce the risk of breath contamination, the sampling set up was attached to 3 m long Teflon 125 tubes, and samples were always taken against air flow direction.

126

The unsaturated zone air was sampled from six boreholes of varying depths between 0.5 and 5 m (Table 1). Spatially, the boreholes cover a large portion of the cave's upstream hydrological catchment, and are overlain by contrasting vegetation cover (mixed-deciduous forest or a grass meadow) (Fig. 1) (Table 1). The gas was sampled in two lines from depths of 0.5 to 130 0.85 m (Shallow 1), three lines from 0.6 to 1.5 m (Shallow 2), and in single lines from a depth of 5 m (Deep 1, Deep 2, Deep 131 3, Deep 4). Due to the nature of the installation, it was not possible to assign a specific depth to the multi-line boreholes. All 132 boreholes were drilled in 2013 and are equipped with aluminium tubes compacted by layers of gravel, bentonite and sand. 133 The sampling line was flushed for 1 min once attached to the borehole, and then samples were taken into the Cali-5-Bond 134 bags. Due to the nature of the borehole installation, we assume that the samples were not taken in steady state conditions, where the production rate of CO₂ would equal the sampling rate.

ID	Well	SISKA	Easting	Northing	Depth	Number of	Classification	Ecosystem
	names	ID	(CH1903+/LV95)	(CH1903+/ LV95)	(m)	sampling lines		cover
			(Swiss grid)	(Swiss grid)				
SG-04	Shallow 1	CO2-13	2'567'083	1'256'904	0.5 to 0.85	2	Soil	Forest
SG-07	Shallow 2	CO2-10	2'567'074	1'257'068	0.6 to 1.5	3	Soil	Meadow
SG-05	Deep 1	EPI-2	2'567'097	1'256'896	5	1	Unsaturated Zone	Forest
SG-10	Deep 2	EPI-4			5	1	Unsaturated Zone	Forest
			2'567'089	1'256'890			Zone	
SG-08	Deep 3	EPI-7	2'567'080	1'257'063	5	1	Unsaturated Zone	Meadow
SG-09	Deep 4	EPI-5			5	1	Unsaturated Zone	Meadow
			2'567'096	1'257'059			Zone	

136

137 Table 1 Summary of the boreholes sampled in Milandre cave catchment noting sample depth, number of sampling lines, 138 classification in soil/ unsaturated zone, and ecosystem cover type. The ID's are the names given to the boreholes for this study, and 139 are concurrent with the supplementary data provided. SISKA (Swiss Institute for Speleology and Karst Studies) IDs refer to the

140 original names of the boreholes at the time of installation.

141 Cave air was sampled in two locations within Milandre cave proximal to both entrances, Downstream (topographically 142 lower) and Upstream (topographically higher), with the same procedure as for the atmospheric samples (Fig. 1). To gain

143 insight into possible spatial variability within the cave, a through trip across the main passage of the cave was carried out in 144 September 2021, and 14 samples were collected (Fig. 1). The trip was taken against the direction of airflow to reduce the risk 145 of breath contamination, from the downstream to upstream entrance.

147 3.2 Continuous O₂ and CO₂ concentration monitoring

148 Soil gas O₂ and CO₂ concentrations were measured continuously nearby Shallow 2 at 40 cm depth and recorded at 10 min 149 intervals between April 2023 and June 2024 using a SCD-41 CO₂ sensor (± 50 ppmV + 5 % of reading) (Sensirion, 150 Switzerland) and SGX-40X O₂ sensor (Amphenol SGX, Sensortech, Switzerland). Calibration was cross-checked with an 151 independent, handheld multi-gas monitor (XAM 5600, Dräger, Germany) before installation.

153 3.3 CO₂ concentration and δ^{13} C analysis

146

152

164

166167

154 The concentration of CO_2 and the stable carbon isotopic composition ($\delta^{13}C$) in all gas samples was measured using a cavity 155 ringdown spectrometer (CRDS) G2131-I Isotopic CO_2 instrument (Picarro, USA) at ETH Zurich (CO_2 concentration = 0.2 156 ppm, $\delta^{13}C = < 0.1$ % precision). Standard gases with known CO_2 concentrations, 399.6 ppmV and 2,000 ppmV CO_2 in 157 synthetic air, were measured in addition to standard gases of known $\delta^{13}CO_2$ values, -27.8 % and -2.8 % VPDB, for offline 158 calibration. As there was no equivalent standard gas available for high CO_2 concentrations as in some samples, linearity of 159 the concentration data produced by the CRDS is assumed. All standards and samples were measured by directly attaching the 160 sample bags to the inlet of the CRDS that was previously fitted with a magnesium perchlorate dryer, and measuring gas 161 concentration and isotopic composition for 2 min after reaching steady state. We used the mean and standard deviation of 162 this measurement interval for evaluation. $\delta^{13}C$ refers to the ratio between the two stable carbon isotopes with respect to the 163 Vienna Pee Dee Belemnite (VPDB) standard:

 $\delta^{13}C \,(\%0) = \left(\frac{\frac{13 \, C}{^{12}C}}{\frac{13 \, C}{^{12}C}} - 1\right) \times 1000 \tag{1}$

168 3.4 Radiocarbon analysis

169 The CO₂ from each gas sample was converted into approximately 1 mg of graphite using an Automatic Graphitization 170 Equipment (AGE, IonPlus, Switzerland) (Wacker et al., 2010a) coupled with a custom-made carbon inlet system. In this 171 process, each sampling bag was successively attached to the inlet system which dried the sample through a fine-grained 172 magnesium perchlorate water trap via a vacuum line. The volume of air required to sample was calculated from the CO₂ 173 concentration of the sample, allowing the appropriate amount of CO₂ to be trapped within a stainless-steel coil that was

174 cooled by submersion in a liquid N_2 bath. After trapping, the CO_2 was sublimated by submerging the coil in a room 175 temperature water bath and then adsorbed onto a zeolite trap using helium as a carrier gas between the coil and the trap. The 176 CO_2 adsorbed onto the trap was then thermally desorbed and filled into the AGE reactor, where it was reduced to graphite 177 with hydrogen over an iron catalyst (Wacker et al., 2010a). A modern standard of Oxalic Acid II gas ($F^{14}C = 1.3407$, Oxa II, 178 NIST SRM 4990C, HEKAL AMS Lab, Hungary) and a radiocarbon fossil reference CO_2 gas ($F^{14}C = 0$, $CO_2 \ge 99.7$ % 179 Vol.abs, Carbagas, Switzerland) were also graphitized and used to calibrate the measurements. The resulting graphite was 180 pressed into targets for radiocarbon analysis through AMS analysis with a MIni CArbon DAting System (MICADAS, 181 Ionplus, Switzerland) (Synal et al., 2007; Szidat, 2020). The resultant radiocarbon data were corrected using the BATS (4.3) 182 software (Wacker et al., 2010b). In this study the ¹⁴C content of samples will be discussed in $F^{14}C$ notation, which represents 183 Fraction Modern (defined as the 1950 atmosphere) according to Reimer et al., (2004):

184

185
$$F^{14}C = \frac{\frac{14 \frac{C}{12_C}}{sample}}{\frac{14 \frac{C}{12_C}}{12_C}}$$
 (2)

186 3.5 Dissolved inorganic carbon analysis

187 Drip water dissolved inorganic carbon (DIC) ¹⁴C was measured to constrain the DIC degassing endmember. Samples were 188 measured over one year from December 2021 and December 2022 at 9 drip sites focused on the actively dripping galleries 189 nearby Upstream and Downstream (Fig. 1). Using a 5 mL syringe, 1 mL of drip water was collected directly from the soda 190 straw stalactites on the cave roof to reduce fractionation effects associated with degassing. The water was injected directly 191 into pre-cleaned Exetainer® (Round Bottom, Borosilicate, 938W, Labco Limited, UK) vials which had been flushed with 192 helium gas and pre-spiked with 150 μL of 85 % H₃PO₄ (Suprapur®, 85 %, Merck KGaA, Germany). The ¹⁴C content of the 193 DIC was measured by sampling the vial headspace using the Carbonate Handling System (CHS, Ionplus, Switzerland) and 194 transferring the gaseous sample to the AMS using a gas handling system. Here, the CO₂ was introduced to the gas ion source 195 through the CHS at a flow of 50 mL min⁻¹. The ¹⁴C content for each sample was measured for ~ 60 cycles. Standard material 196 with a carbonate matrix of similar composition to the DIC samples were used as standards (IAEA C1 (F¹⁴C = 0) and C2 197 (F¹⁴C = 0.411), sodium bicarbonate (NaHCO₃, Sigma Aldrich, USA) and potassium bicarbonate (KHCO₃, Sigma Aldrich, 198 USA) (both F¹⁴C = 0)).

199

200 3.6 Data analysis and statistics

201

202 All data and statistical analyses and all graphs were generated using the Python 3 programming language (Van Rossum & 203 Drake, 2009).

205 Relationships between CO_2 concentration, $\delta^{13}C$, $F^{14}C$ for each sample type and the Mean Monthly Temperature (MMT) and 206 Mean Monthly Precipitation (MMP) from Fahy weather station were explored using Spearman's rank correlation coefficient 207 analysis (Kokoska & Zwillinger, 2000). A significantly correlated relationship between two variables is defined by p < 0.05, 208 with the correlation coefficient denoted by "rho", and number of samples involved in the analysis as "n".

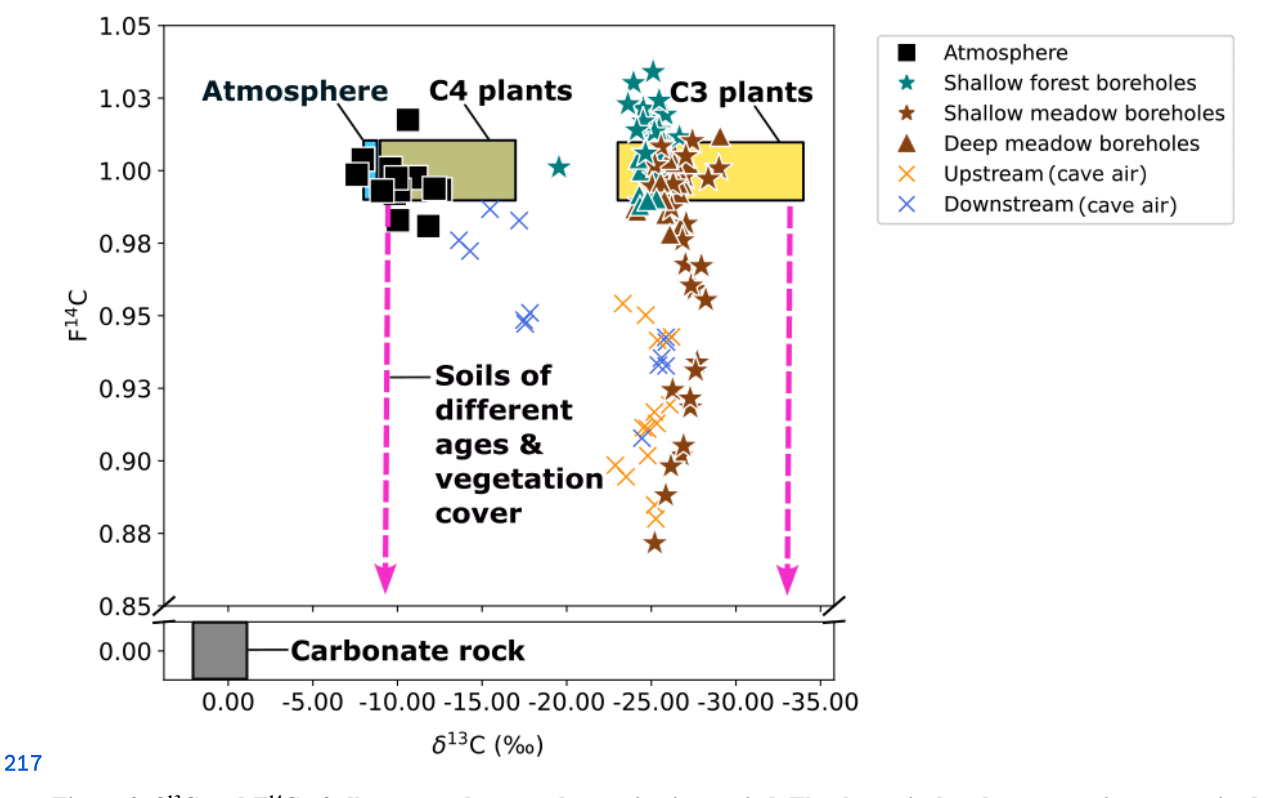
210 4 Results

209

211 4.1 Atmospheric CO₂

212 The atmospheric samples had a CO_2 concentration ranging from ~ 380 ppmV (August 2023) to ~ 485 ppmV (December 213 2022) with a mean of ~ 440 ppmV. The δ^{13} C ranged from -12.5 ‰ (February 2023) to -7.6 ‰ (August 2023) and had a mean 214 of -10.1 ‰ (n = 17). The CO_2 sampled was typically modern, though had some fluctuation from F¹⁴C 0.98 (December 2022) 215 to 1.02 (June 2022) and a mean of F¹⁴C 1.0 (Fig. 2).

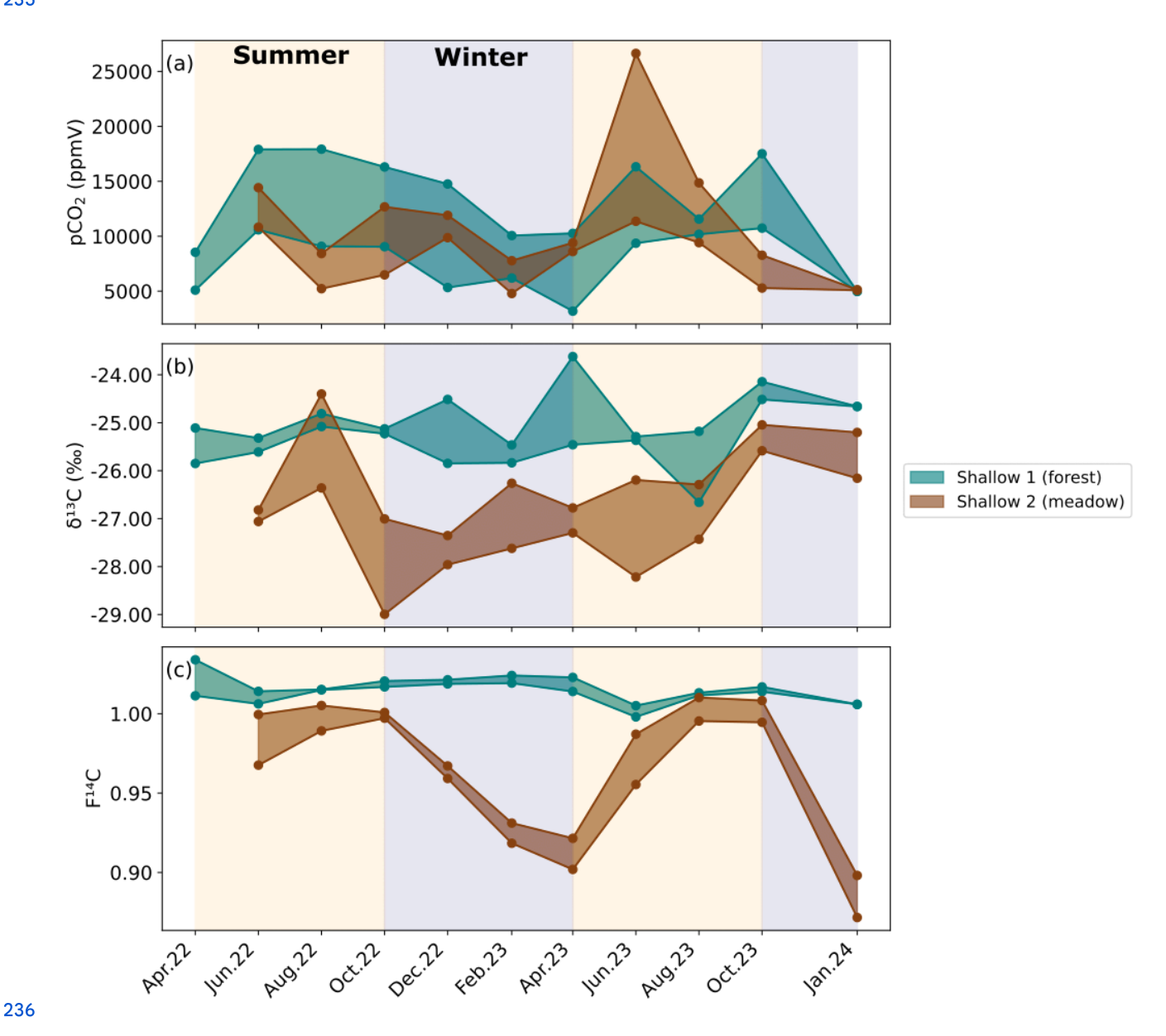




218 Figure 2. δ^{13} C and F¹⁴C of all gas samples over the monitoring period. The theoretical carbon reservoirs present in the system are 219 shown with the atmosphere (blue), C3 plants (yellow), C4 plants (green), soils of various ages and compositions (pink arrows), and 220 carbonate rock (grey).

221 4.2 Soil Zone CO₂

- 222 Soil boreholes have higher CO_2 concentrations and lower $\delta^{13}C$ compared to the atmosphere (Fig. 2). Concentrations in 223 boreholes that sample the soil zone (Shallow 1 and Shallow 2) (Fig. 3a) vary significantly depending on sampling depth, 224 cover type, and season. The Shallow 1 boreholes (forest) show seasonal high p CO_2 in the summer months from June to 225 October, which steadily declines during winter until it begins to rise again after April. In these boreholes CO_2 concentrations 226 vary from a maximum of $\sim 18,000$ ppmV in August 2022 to a minimum in January 2024 of $\sim 1,200$ ppmV, with a mean of 227 $\sim 10,700$ ppmV (n = 21). The CO_2 concentrations in Shallow 2 (meadow) boreholes range from $\sim 27,000$ ppmV in June 2023 to $\sim 4,800$ ppmV in February 2023 with a mean of $\sim 9,900$ ppmV (n = 30).
- 229
- 230 The $\delta^{13}C$ varies by 7.0 % in shallow forest boreholes over the sampling period ranging from a minimum of -26.7 % in
- 231 August 2023 to a maximum of -19.5 ‰ in January 2024 (Fig. 3b). There is ~ 4.0 ‰ isotopic variation in the shallow
- 232 meadow boreholes with a minimum of -29.0 % in October 2022 and a maximum of -24.4 % in August 2022. The pCO₂ and
- 233 δ^{13} C are negatively correlated in both shallow forest and shallow meadow boreholes (forest: rho = -0.47, p = 0.02, n = 25.
- 234 meadow: rho = -0.49, p = 0.01, n = 30), and δ^{13} C is on average lower in shallow meadow than shallow forest boreholes.



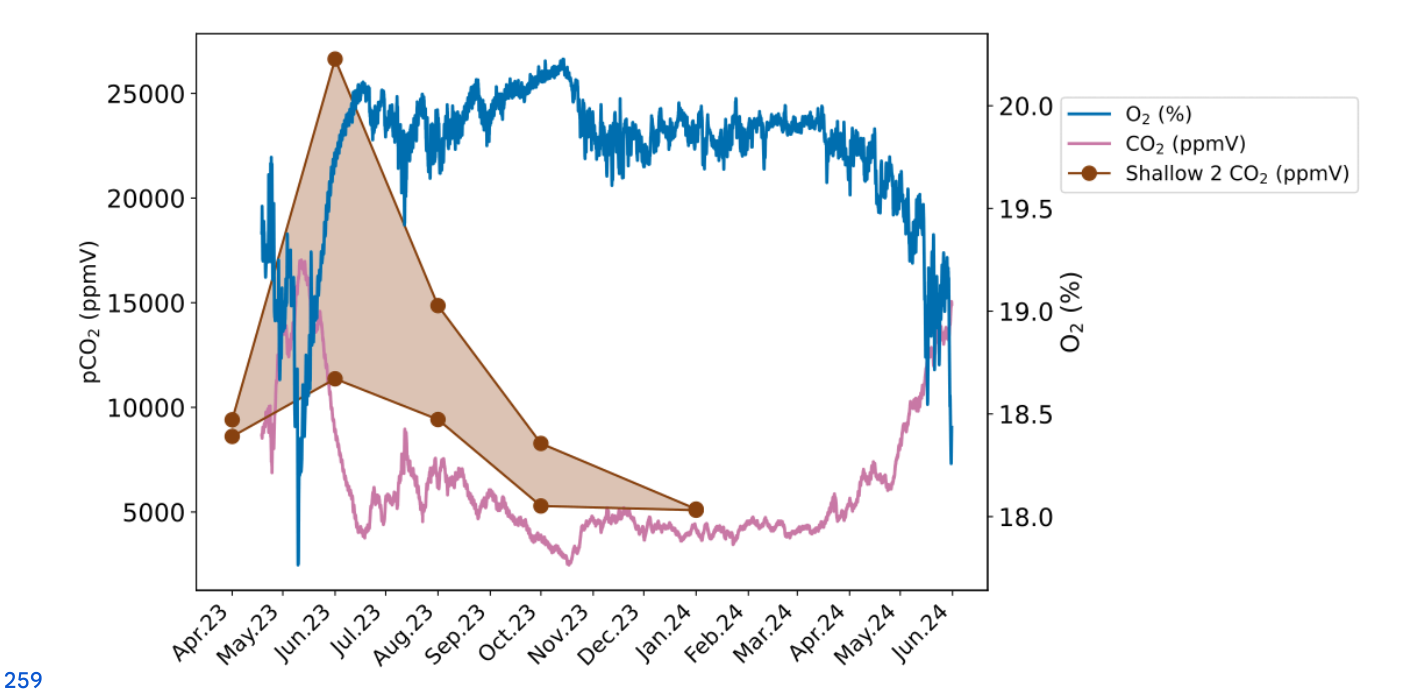
237 Figure 3. Maximum and minimum a) CO_2 concentration, b) $\delta^{13}C$ and c) $F^{14}C$ of the three soil borehole samples from Shallow 1 in 238 the forest (green), and the two sampling lines in Shallow 2 in the meadow (brown). Summer (yellow) and winter (blue) seasons are 239 highlighted by the coloured background. Concentrations are shown as ranges between maxima and minima as they aggregate over 240 three sampling lines in the soil per location (Table 1).

243 F¹⁴C in Shallow 1 boreholes (forest) shows little annual variability and fluctuates slightly around a modern value (max = 244 1.03 in April 2022, min = 1.0 in June 2023) (Fig. 3c). Conversely, the shallow 2 (meadow) boreholes show distinct annual 245 variation in F¹⁴C, which steadily decreases from modern (1.0) in August 2022 and 2023 to a low in April 2023 and a 246 minimum in January 2024 (0.87). The samples from the shallow forest boreholes have a positive correlation between F¹⁴C 247 and δ ¹³C (rho = 0.48, p = 0.02, n = 25). In the shallow meadow borehole samples, we observe a positive correlation between 248 F¹⁴C and MMT (rho = 0.67, p = 0.001, n = 30). All other tested parameters show no significant correlations (see Appendix 249 A).

250

The continuously measured O_2 and CO_2 concentrations nearby Shallow 2 in the meadow show an inverse relationship (Fig. 4). The concentrations are relatively stable throughout most of the year with higher O_2 and lower CO_2 concentrations. This pattern is disturbed by a sharp decrease in O_2 and an increase in CO_2 observed around May/June of both 2023 and 2024. These different conditions last around one month before returning to the typical concentrations. The O_2 concentration ranges from a maximum of 20.2 % in August 2023 to a minimum of 17.8 % during a brief interval in May 2023. Conversely, the CO_2 concentration peaks at \sim 17,000 ppmV in May 2023 and is the lowest at \sim 2,500 ppmV in August 2023. The Shallow 2 boreholes also show peaks in CO_2 concentration in May to June 2023 (Fig. 4).

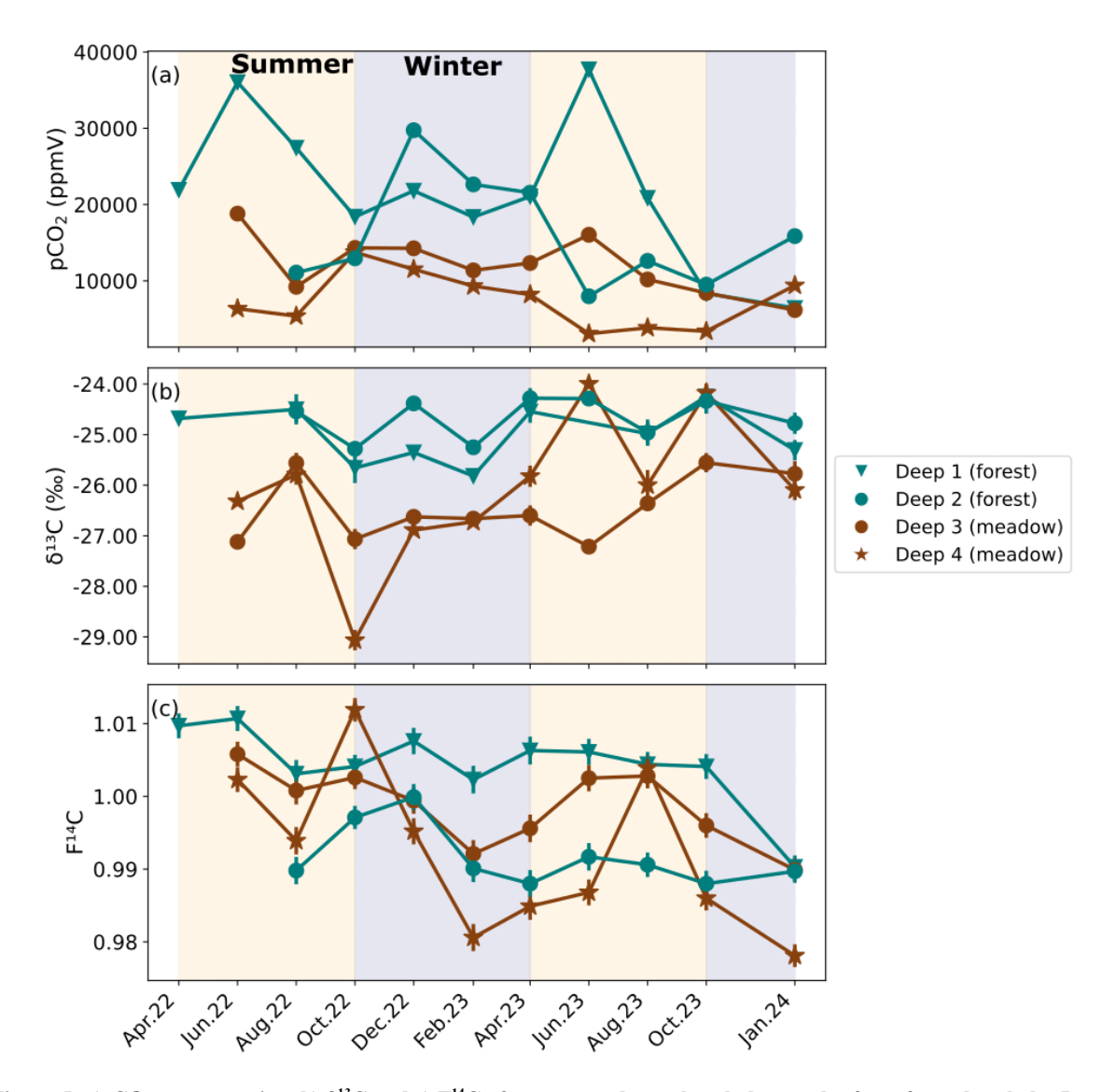
258



260 Figure 4. Continuously measured CO_2 (pink) and O_2 (blue) concentrations from the soil zone nearby the Shallow 2 261 boreholes. CO_2 concentrations from Shallow 2 are also plotted (brown).

264 4.3 Unsaturated Zone CO₂

- 265 Unsaturated zone CO_2 concentrations varied widely during the sampling period but are generally very high (>10,000 ppmV). 266 On average, the forest boreholes Deep 1 and Deep 2 have higher concentrations than the meadow boreholes Deep 3 and 267 Deep 4. Concentrations are generally highest in the Deep 1 borehole (forest) (Fig. 5a) with a maximum of ~ 37,000 ppmV in 268 June 2023 and a similarly high concentration peak in June 2022. The lowest values (~ 21,000 ppmV) at this borehole are 269 recorded in the winter months. Deep 2 (forest) shows an opposite trend with its highest CO_2 concentrations in autumn, 270 winter, and spring (max = ~ 29,000 ppmV in December 2022). The lowest CO_2 concentrations were measured during the 271 summer months (min = ~ 7,900 ppmV in June 2023). There is comparatively less variability in the Deep 3 and Deep 4 272 boreholes (both in the meadow). In Deep 3, concentrations fluctuate from ~ 6,100 to ~ 19,000 ppmV with no obvious 273 seasonality. Deep 4 has higher concentrations over the winter period and lower during summer, peaking at ~ 14,000 ppmV in 274 October 2022 and dropping to an overall minimum of ~ 3,000 ppmV in June 2023.
- 276 The δ^{13} C of the majority of unsaturated zone CO_2 samples is very stable around \sim -26 ‰ (Fig. 5b). Similar to the shallow 277 boreholes, samples from deep meadow boreholes (Deep 3 and 4) have on average slightly lower δ^{13} C values. In the meadow 278 boreholes Deep 3 and Deep 4, the δ^{13} C and pCO₂ are negatively correlated (rho = -0.66, p = 0.001, n = 21) (see Appendix A). 279



281 Figure 5. a) CO_2 concentration, b) $\delta^{13}C$ and c) $F^{14}C$ of unsaturated zone borehole samples from forest boreholes Deep 1 and Deep 2 (green), and meadow boreholes Deep 3 and Deep 4 (brown). Summer (yellow) and winter (blue) seasons are highlighted by the 283 coloured background.

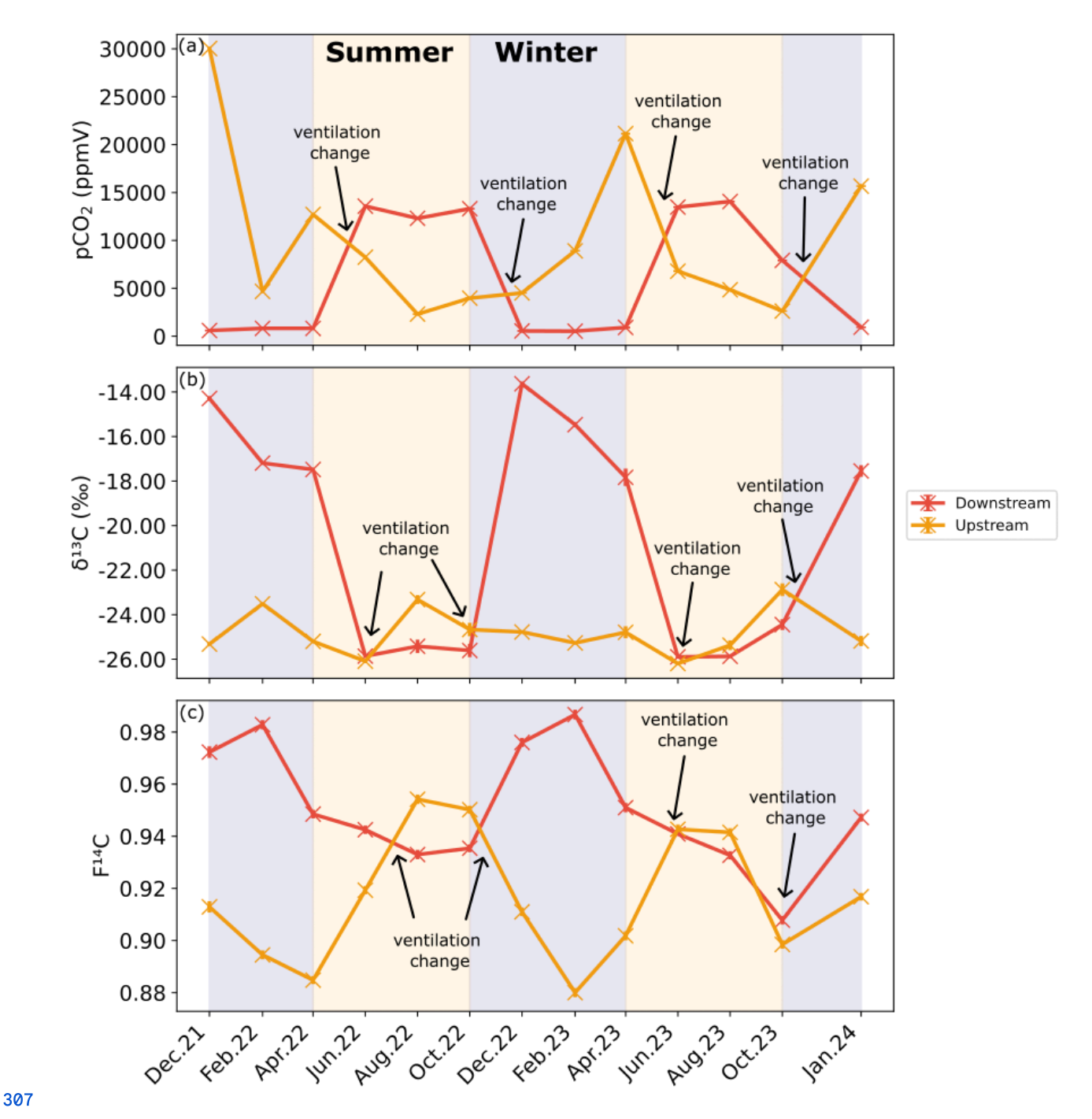
290

284 The F¹⁴C of unsaturated zone CO₂ samples is relatively stable throughout the sampling period, ranging from 1.01 (Deep 1, 285 June 2022) to 0.98 (Deep 4, October 2022) (Fig. 5c). A possible seasonal pattern can be observed in the meadow boreholes 286 (Deep 3 and Deep 4) with lower F¹⁴C values in the winter and spring months and higher F¹⁴C during summer, similar to the 287 observation from the shallow meadow boreholes. No clear seasonal pattern is observed for Deep 1 and Deep 2. The F¹⁴C 288 values of unsaturated zone CO₂ samples are negatively correlated with their δ^{13} C value (rho = -0.54, p = 0.01, n = 21) and 289 positively correlated with MMT (rho = 0.53, p = 0.01, n = 21). All other tested parameters show no significant correlations.

291 4.4 Cave CO₂

306

292 The CO_2 concentrations at the Downstream and Upstream sampling points in the cave are inversely correlated (Fig. 6a).
293 Downstream shows a higher pCO₂ from June to October in 2022 and 2023, with a maximum of ~ 14,000 ppmV in August
294 2023. The lowest concentrations are seen between December and April, reaching near atmospheric concentrations with a
295 minimum of ~ 420 ppmV in December 2021. Conversely, the highest CO_2 concentrations at the Upstream site were
296 measured during the winter months, with a maximum of ~ 30,000 ppmV in December 2021. The lowest CO_2 concentrations
297 at Upstream were observed during the summer months with a minimum of ~ 2,300 ppmV in August 2022. Overall,
298 concentrations at the Upstream site reach higher maxima and do not approach atmospheric values at their minimum, as at the
299 Downstream site. The isotopic composition of CO_2 is inversely related to its concentration, with higher CO_2 concentrations
300 coinciding with lower $F^{14}C$ and $\delta^{13}C$ values. Seasonal trends differ between sites, at the Downstream site $\delta^{13}C$ and $F^{14}C$ 301 values are higher in winter and lower in summer, whereas at the Upstream site, $\delta^{13}C$ and $F^{14}C$ values show the opposite
302 pattern (Fig. 6b and c). The $\delta^{13}C$ in Downstream ranged between -25.9 % in June 2023 and -13.6 % in December 2021, and
303 the $F^{14}C$ between 0.91 in October 2023 and 0.98 in February 2023. At Upstream, the opposite relation with CO_2 304 concentration is well expressed for $F^{14}C$, but not as clear for $\delta^{13}C$, with minimal variability over the entire study period. The
305 $\delta^{13}C$ in Upstream fluctuates slightly around a mean of -24.8 %.

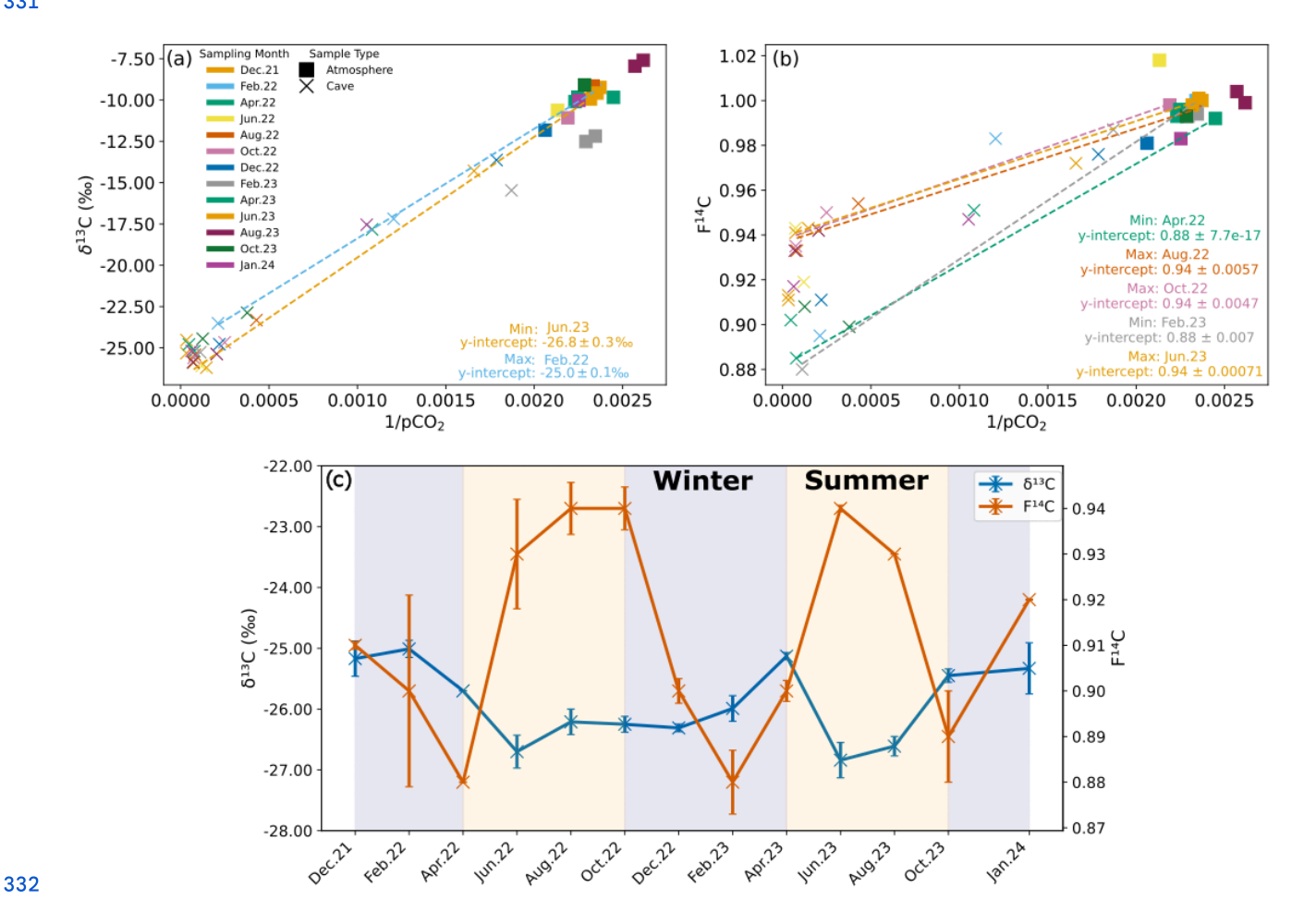


308 Figure 6. a) CO_2 concentration, b) $\delta^{13}C$ and c) $F^{14}C$ of cave air samples from the Downstream (red) and Upstream (orange) sites. 309 Summer (yellow) and winter (blue) seasons are highlighted by the coloured background. The approximate timing of the 310 temperature driven ventilation direction changes are shown by the annotations.

312 The $F^{14}C$ of CO_2 in Upstream is overall lower than that of Downstream, increasing over late spring 2022 and into summer, 313 peaking during August 2022 at 0.95. Decreasing $F^{14}C$ is observed during winter and into spring with lows of ~ 0.88 in 314 February 2023. At the Downstream site, the pCO_2 and $\delta^{13}C$ (rho = -0.9, p = 0.0001, n = 14), pCO₂ and $F^{14}C$ (rho = -0.83, p = 315 0, n = 14), and $\delta^{13}C$ and MMT (rho = -0.79, p = 0.0001, n = 14) are negatively correlated. Moreover, the pCO_2 and MMT 316 (rho = 0.53, p = 0.05, n = 14), and $\delta^{13}C$ and $F^{14}C$ (rho = 0.74, p = 0, n = 14) are positively correlated. At the Upstream site, 317 pCO₂ and MMP are positively correlated (rho = 0.55, p = 0.04, n = 14), and pCO₂ and MMT are negatively correlated (rho = 318 -0.54, p = 0.05, n = 14) (See Appendix A). All other tested parameters show no significant correlations.

319

To constrain the isotopic composition of the end members contributing CO_2 to the cave air mixture, we use the Keeling plot approach (Fig. 7a & b). This approach assumes that cave air is a mixture of two main sources, the atmosphere (with known concentration and isotopic values), and a second source of a priori unknown composition. The y-intercepts of the Keeling plots represent the isotopic composition of the contributing end member which mixes with atmospheric air inside the cave (Keeling, 1961; Pataki et al., 2003) (Fig. 7a & b). We find that over time, the isotopic composition of the endmember varies for both $\delta^{13}C$ and $F^{14}C$ (Fig. 7c). The endmember $\delta^{13}C$ value varies by ~ 2.0 % from -26.8 % in June 2023 to -25.0 % in February 2022. The variation in the $F^{14}C$ is larger, ranging from 0.88 in February 2023 to 0.94 in June 2022, August 2022, October 2022, and June 2023 (ca. ~ 0.06 $F^{14}C$). Maxima in the $F^{14}C$ value derived for the endmember through the Keeling plot generally correspond to decreases in $\delta^{13}C$, with two $F^{14}C$ maxima occurring in June to October 2022 and in June to August 2023.

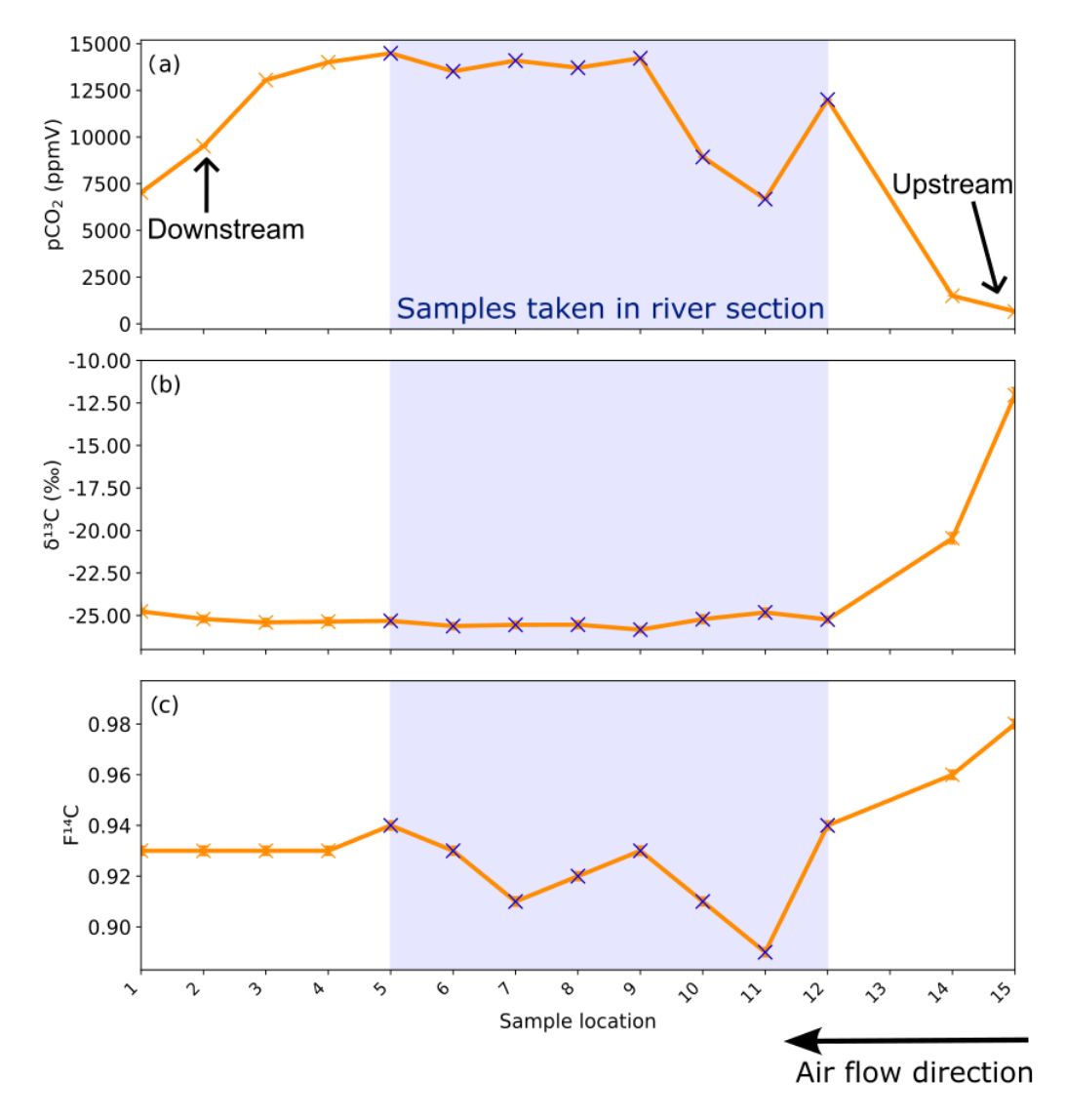


333 Figure 7. Keeling plots for $\delta^{13}C$ (a) and $F^{14}C$ (b) of cave (Upstream and Downstream sites) and atmospheric samples from all 334 monitored months. The dashed regression lines denote the months with the maximum and minimum y-intercepts for $\delta^{13}C$ and 335 $F^{14}C$. c) Keeling plot y-intercepts for $\delta^{13}C$ (blue) and $F^{14}C$ (orange) over time. Summer (yellow) and winter (blue) seasons are 336 highlighted by the coloured background.

338 Samples taken along the main passage of the cave during the through trip show increasing pCO₂ from the lower entrance 339 (location 1, corresponding to Downstream monitoring site, ~ 6,900 ppmV) to a plateau of ~ 14,000 ppmV from sample point 340 4 to 9 towards the centre of the cave (Fig. 8a). The pCO₂ decreases sharply after sample point 9 until point 11 (~ 6,600 341 ppmV). The pCO₂ increases briefly at sample point 12 and then decreases again upon approach to the cave exit (Upstream). 342 The δ^{13} C values remain essentially constant at -25.5 % through the initial segments of the cave, beginning to increase 343 slightly past sample point 9 (Fig. 8b). The δ^{13} C value is -25.8 % at sample point 9 and progressively increases as pCO₂ levels 344 drop between sampling points 9 and 11, followed by a strong increase toward the Upstream exit (-11 ‰). The F¹⁴C values 345 are constant at ~ 0.93 between sample points 1 and 5, followed by more variability and generally lower F¹⁴C values in the

346 middle of the transect, coinciding with the river passage of the cave (minimum 0.89 at sampling point 11; Fig. 9c). Towards 347 the Upstream exit, F¹⁴C begins to increase strongly (maximum 0.98 at sampling point 15; Fig. 8c). Sample 13 is excluded 348 due to a ruptured bag during sampling.





351 Figure 8. a) CO_2 concentration, b) $\delta^{13}C$ and c) $F^{14}C$ of cave air samples from the different sites sampled during the through trip. 352 Sampling locations are shown in Fig. 1. The blue crosses and blue bar notate where samples were taken standing in the river. The 353 direction of cave air ventilation is shown by the lower arrow. The approximate locations of the Upstream and Downstream 354 sampling sites are annotated.

355 5 Discussion

356 5.1 Sources and variability of shallow depth CO₂

357 The observed fluctuations in CO₂ concentrations in the Shallow borehole gas samples vary with depth, vegetation cover, and 358 season (Fig.3), suggesting complex carbon cycling dynamics taking place in the soil zone and shallow fractured epikarst. 359 Overall, both samples from forest and meadow locations have similar mean CO₂ concentrations. In the Shallow 1 forest 360 boreholes, higher CO₂ concentrations occur during summer months (Fig. 3a), aligning with increased autotrophic (occurring 361 in plant roots, leaves, and stems) and heterotrophic (microbial) respiration rates during warmer seasons. This results in 362 higher CO₂ production compared to losses from soil efflux to the atmosphere and downward transport in gaseous or 363 dissolved form. Due to our discrete sampling approach, we cannot discern whether higher production or decreased losses are 364 responsible for higher CO₂ concentrations. The decline in CO₂ concentrations during winter suggests that reduced 365 autotrophic and soil microbial respiration in response to lower temperatures is likely an important driver of the seasonal 366 cyclicity. The lower CO₂ concentrations during winter in the forest boreholes (Shallow 1) compared to the meadow 367 boreholes (Shallow 2) could be an indication of frost effects. Soil frost induced by colder temperatures can reduce 368 heterotrophic respiration in soils. Experiments inducing deep frost in forested soils by removing snow cover caused a greater 369 decrease in heterotrophic respiration during winter months compared to snow covered control soils (Muhr et al., 2009). 370 Furthermore, frost-heave can physically damage the extraradical hyphae on plant roots (Lekberg & Koide, 2008). Due to the 371 shielding of the tree canopy, the forested areas in the Milandre catchment likely experience less snow cover compared to the 372 open meadow where snow can accumulate freely. The meadow soils may experience reduced frost effects, meaning that 373 heterotrophic respiration is not impacted to the same extent as the forest soils and can accumulate CO₂ year-round, as seen in 374 borehole Shallow 2. However, during the monitored period, the Milandre catchment experienced little snow cover, 375 suggesting that frost effects were likely minimal overall.

376

377 Though CO₂ production is reduced in winter, concentrations of several ~1,000 ppmV are measured at our sites, perhaps due 378 to: i) slow, but persisting metabolic microbial activity at low temperatures (possible even below freezing temperatures as low 379 as -5 to -7.5 °C (Kähkönen et al., 2001)), ii) reduced, but persisting autotrophic respiration of shallow roots, or iii) because of 380 reduced transportation of CO₂ due to higher soil water content (Hashimoto & Komatsu, 2006). Similar seasonal trends in 381 CO₂ concentrations have been reported in other studies (Billings et al; 1998; Pumpanen et al., 2003; Zhang et al., 2023).

382

383 The δ^{13} C values of CO₂ in shallow boreholes located in both the meadow and forest correspond to the typical isotopic 384 signature of C3 plants which dominate the catchment area, supporting our interpretation of a dominant biogenic source of 385 carbon in the soil gas (Fig. 2) (Fig. 3b). Plants using the C3 metabolic pathway (e.g. most temperate vegetation) produce 386 carbon with a δ^{13} C of \sim -23 to -34 % (Staddon et al., 2004). Furthermore, due to the nature of the sampling, the soil was not 387 sampled in steady state conditions, potentially disturbing any existing CO₂ trends with depth. Another consideration is the

388 symbiotic relationship between arbuscular mycorrhizal fungi (AMF) and plant roots which is ubiquitous globally, occurring 389 in 80 % of terrestrial plants (Fitter et al., 2000). AMF grows on plant roots and forms arbuscules within root cells, and 390 hyphae which extend into the soil (Zhu & Miller, 2003). Plants benefit from this relationship because of the increased uptake 391 of nutrients such as phosphorus and nitrogen, and improved resistance to environmental stress through more stable soil 392 structure and enhanced water absorption (Kiers et al., 2011; Boyno et al., 2024). The fungi benefit through access to plant 393 derived carbohydrates for energy, and a stable environment for growth and reproduction (Kiers et al., 2011). The respiration 394 of AMF can contribute to the subsurface sequestration of carbon (Treseder & Allen, 2008), and may indeed contribute to the 395 subsurface CO₂ which we measured at Milandre cave. There appears to be a temperature dependance of roots with AMF 396 colonisation, where respiration rates increase at higher temperatures (Atkin et al., 2008). We observe an increase in CO₂ 397 concentration during the higher temperature summer months (Fig. 3a, Fig. 5a), which may be caused in part by a 398 contribution of CO₂ from enhanced respiration of AMF. The isotopic composition of the CO₂ produced by AMF respiration 399 is not currently well constrained. Studies analysing the δ^{13} C of individual AMF spores showed that the δ^{13} C broadly 400 corresponded to the C3 or C4 plant that it was associated with (Nakano et al., 1999). Therefore, it can be assumed that CO₂ 401 produced by AMF respiration is similar to that of the C3 host plant dominated catchment of Milandre cave. As carbon is 402 fixed from modern atmospheric CO₂ during host plant photosynthesis, the F¹⁴C signature should be modern (~1). Hence, the 403 respiration of AMF may contribute to the modern CO₂ measured in the boreholes in both meadow and forest sites (Fig.3 & 404 5).

405

406 Though both meadow and forest boreholes have C3 plant δ^{13} C signatures, the δ^{13} C values of CO₂ in meadow soils are on 407 average lower than those in the forest soils. Previous analysis of soil CO₂ from various karstic sites in Slovenia showed a 408 similar trend, whereby the δ^{13} C values in meadow sites were ~1 ‰ lower compared to forested sites (Stickler et al., 1997). 409 The meadow and forested areas at our site have developed contrasting soil compositions, with the meadow soils deeper, 410 more compacted, and with a higher organic content than the forest soils, which are shallow, unconsolidated, and with more 411 roots. Comparisons of root free and root containing soils have suggested that root respiration contributes lower δ^{13} CO₂ to the 412 soil gas (Diao et al., 2022). This is the opposite trend to what our findings would suggest. Efforts to disentangle the δ^{13} C of 413 autotrophic and heterotrophic contributions to soil CO₂ have shown a range of results, where autotrophic respiration can 414 produce the same (Wu et al., 2017), higher (Moyes et al., 2010), or lower (Risk et al., 2012) δ^{13} C than heterotrophic 415 respiration. However, different soil compositions can affect soil moisture, which can cause both increases (Unger et al., 416 2010), decreases (Powers et al., 2010), and no change (Diao et al., 2022) in soil δ^{13} C. It is therefore difficult in the context of 417 this study to determine the exact reason for the difference in δ^{13} C between surface covers. Interestingly, we also do not find 418 evidence for contributions to subsurface gas from C4 plants, possibly due to the absence of sampling locations in the fields in 419 the catchment where C4 crops are grown, suggesting limited lateral gas transport.

421 The CO₂ F^{14} C of meadow boreholes in Shallow 2 shows statistically significant seasonal behaviour (rho = 0.67, p = 0.001, n 422 = 30), with more aged CO₂ dominating the winter and spring months ($F^{14}C \sim 0.88$), and modern CO₂ in summer ($F^{14}C \sim 0.88$). 423 1.00) (Fig. 3c). These seasonal shifts suggest a potential influence of temperature-sensitive processes on soil carbon 424 dynamics, with higher autotrophic respiration rates and heterotrophic respiration of very recently fixed photosynthates 425 dominating in the warm months (Campeau et al., 2019). Though typically the productive growing season for meadow 426 grasses occurs in spring (Wingler & Hennessy, 2016), there is a lag in the F¹⁴C response, which peaks between June and 427 October. This may be due to the time it takes for enough modern CO₂ to accumulate in the soil and dominate the average gas 428 age. Similar impacts of seasonality on the contributions of young carbon pools to the soil CO₂ budget have been observed in 429 soils of various environments whereby autotrophic respiration and heterotrophic decomposition of younger carbon dominate 430 in warmer months (Trumbore, 2000; Chiti et al., 2011; Vaughn & Torn, 2018). A contribution of fossil carbon from the 431 dissolution of carbonate bedrock fragments in the soil zone could also be considered to explain the low soil CO₂ F¹⁴C values 432 in winter. However, such a bedrock contribution would result in a concomitant increase in δ^{13} C, as marine carbonates, which 433 typically constitute the karstified host rock, are characterized by δ^{13} C of values of ~ 0 % (Planavsky et al., 2015) and up to + 434 2 ‰ in the region of Milandre cave (Weissert & Mohr, 1996) (Fig. 2). This would contribute a gaseous δ^{13} C ~ 9.54 ‰ lighter 435 when at equilibrium with DIC from carbonate dissolution at 10.5 °C (Mook et al., 1974). Since we do not observe increases 436 in δ^{13} C of soil gas during the periods of lower F^{14} C, this is an unlikely scenario. A further explanation for the seasonal 437 variability could be due to the seasonal ventilation dynamics in the karst system, which promote upward movement of cave 438 air during the winter, and downwards movement of soil air in summer (see section 5.4).

439

440 The modern $F^{14}C$ CO_2 signature in the Shallow 1 forest borehole (Fig. 3c) suggests a year-round dominant source of CO_2 441 from autotrophic root respiration and the decomposition of very recently fixed soil organic matter. As the root systems are 442 deeper and more developed in the forest soils, there is a higher input of modern carbon compared to the meadows. The soils 443 in the forested area are shallow (in some areas < 10 cm deep) and are dominated by large pebbles and fragments of the 444 carbonate bedrock and shallow roots. Thus, shallow depth carbon sequestration may be suppressed in the forest soil, 445 resulting in a CO_2 profile dominated by deeper root respiration (Hasenmueller et al., 2017; Tune et al., 2020).

446

447 5.2 Sources and variability of CO₂ at 5 m depth

448 CO₂ concentrations at 5 m depth vary considerably over the sampling period and between individual sites (Fig. 5a). CO₂ 449 concentrations are generally higher in the forest boreholes (Deep 1, Deep 2) than in the meadow boreholes (Deep 3, Deep 4), 450 likely due to the high volumes of CO₂ produced by autotrophic respiration of the mature woodland root system which 451 penetrates deep into the unsaturated zone. The CO₂ δ^{13} C values across all boreholes reflect the C3 dominated ecosystem of 452 the catchment, and do not indicate any input from C4 plants in the nearby fields. Notably, the ecosystem composition of the 453 overlying vegetation (meadow vs. forest) influences the isotopic composition of CO₂ at 5 m in the same way as the shallow 454 boreholes, with a slightly lower δ^{13} C values in the meadow than the forest. The F¹⁴C values of unsaturated zone CO₂ vary

455 across all deep boreholes by \pm 0.02 around a mean value of 1.00 (Fig. 5c), suggesting that across the catchment, autotrophic 456 tree root respiration may be the dominant source of CO_2 at these depths (Breecker et al., 2012; Tune et al., 2020). 457 Furthermore, the year-round modern CO_2 F¹⁴C values in the deeper meadow boreholes Deep 3 and Deep 4 compared to the 458 seasonally pronounced signal in the shallower boreholes of Shallow 2 highlights the potential influence of the meadow 459 doline morphology. Boreholes Deep 3 and Deep 4 were drilled on the edge of the doline beneath shallow leptosols like those 460 found in the forest, while Shallow 2 was drilled fully within the doline, where the soil is thicker and much richer in organic 461 matter. Unfortunately, there is no unsaturated zone depth borehole installed within the lower basin of the meadow to verify 462 whether the seasonal signal measured at Shallow 2 translates to the deeper subsurface.

463

464 Whilst many studies point to the degradation of exported aged organic matter being the main source of karstic ground air 465 (Breecker et al., 2012; Mattey et al., 2016; Bergel et al., 2017), unsaturated zone borehole CO₂ in the Milandre cave 466 catchment has predominantly modern F¹⁴C values, and does not show seasonal isotopic variability. This suggests that the 467 majority of the CO₂ at 5 m depth is likely supplied by contemporaneous C3 tree root respiration. Similarly modern (106.4 pMC (percent modern carbon, corresponding to 1.064 in F¹⁴C)) biologically sourced CO₂ was also detected in boreholes 469 from Nerja cave, Spain (Vadillo et al., 2016). Modern, but not substantially above modern F¹⁴C also excludes the 470 contribution of substantial amounts of decadal-aged soil material containing bomb spike carbon due the enrichment in ¹⁴C by 471 thermonuclear weapons testing during 1950's and 1960's (Trumbore, 2000; Shi et al 2020). This result supports the body of 472 literature stating that, in addition to the export and respiration of older carbon, large volumes of modern carbon are also 473 transported into the unsaturated zone, likely in large part through deep root respiration (Breecker et al., 2012; Campeau et al., 474 2019; Tune et al., 2020). This suggests that deep roots, as found in mature forest ecosystems, might be more important than 475 previously thought in contributing to the ground air budget.

476 5.3 Ventilation driven isotopic variation in cave air

477 The CO_2 dynamics in the cave show distinct variations in concentration and isotopic composition between the two sampling 478 points Upstream and Downstream (Fig. 6a, b, c). Cave ventilation dynamics modulate the mixing ratio between the 479 atmosphere and the other contributing pools, and are usually the dominant source of variability (Kukuljan et al., 2021; 480 Buzjak et al., 2024). Recent modelling of air flow dynamics in Milandre cave found that outside temperature controls 95 % 481 of flow variability (Garagnon et al., 2022). During colder months when the outside temperature is ≤ 8 °C, the air in the cave 482 flows topographically upwards from the northern downstream entrance close to the Downstream site, to the higher entrance 483 closer to Upstream. When the temperature increases above 8 °C, the ventilation regime reverses. This seasonality is reflected 484 in the alternating concentrations and isotopic composition of the CO_2 at the cave sampling sites as they experience varying 485 amounts of dilution with atmospheric air during the year. CO_2 degassing from the cave river at Upstream reduces the dilution 486 effect in the upper passage. The effects of ventilation can also be observed in the higher spatial resolution sampling during 487 the through trip (Fig. 8a, b, c) whereby the summer regime ventilation resulted in lower concentrations, more positive $\delta^{13}C$,

488 and increased $F^{14}C$ due to atmospheric mixing closer to the upper entrance (Upstream site). Spatially, a marked decrease in 489 CO_2 concentration and $F^{14}C$ occurs at sampling locations 10 and 11 (~750 to 1,000 m from the cave entrance respectively) 490 though little change is observed in the $\delta^{13}C$. This air input could be associated with an older organic matter pool which, 491 however, contributes only little to the entire CO_2 mass flux.

492

493 5.4 Sources and variability of CO2 in cave air

494

495 The Keeling plot y-intercepts show that the composition of the gas pool (karst endmember) that mixes with atmospheric air 496 in the cave varies seasonally (Fig. 7c). It is important to note that, while the isotopic composition of cave CO_2 is influenced 497 by ventilation-driven dynamics, the Keeling plot y-intercept represents the composition of the subsurface gas that mixes with 498 the atmospheric air during ventilation and is not affected by it. The $\delta^{13}C$ of the karst endmember is mostly stable, varying ± 2 499 % around a mean value of -26 %, a value typically associated with the CO_2 produced by the C3 plants which dominate the 500 catchment ecosystem. This value is also very similar to the $\delta^{13}C$ CO_2 values of soil and unsaturated zone gas and reinforces 501 the notion of the karst endmember being dominated by ecosystem respiration. Previous work at Milandre cave investigating 502 aquifer dynamics using 222 Rn suggested that the majority of the cave CO_2 comes from the overlying soils (Savoy et al., 503 2011). The $F^{14}C$ of the Keeling plot y-intercept, on the other hand, shows seasonal variability with distinctly more "modern" 504 (closer to $F^{14}C = 1$) during the summer and "aged" ($F^{14}C < 1$) CO_2 during the winter. The transition from an $F^{14}C$ of 0.94 to 505 0.88 represents a change in the mean apparent age of CO_2 from ~ 100 to 1000 years, well beyond the assumed residence time 506 of water in the unsaturated zone of ~ 5.5 to 6.6 years (Affolter et al., 2020).

507

508 Several mechanisms may be responsible for the seasonal $F^{14}C$ fluctuations of the karst endmember. A contribution of carbon 509 from the oxidation of methane, either from methanotrophs or through the evolution of pore fluid waters, must be considered. 510 Methane can be produced by both thermogenic (originating from ancient organic rich sediments) and biogenic (particularly 511 through methanotrophic bacteria) processes (Suess & Whiticar, 1988). The $\delta^{13}C$ CO₂ range of published values for the CO₂ 512 resulting from methane oxidation from both sources is broad, with biogenic spanning from \sim - 20 to -90 ‰, and thermogenic 513 from \sim -30 to -65 ‰ (Suess & Whiticar, 1988). The $\delta^{13}C$ CO₂ produced by thermogenic sources can also evolve to less 514 negative values of \sim - 25 to - 34 ‰ in settings where there is near total conversion of CH₄ to CO₂ (Shoell, 1980; Frieling et 515 al., 2016). Methane that undergoes biogenic oxidation is typically sourced from the atmosphere, meaning the resulting CO₂ 516 will have a modern $F^{14}C$ signature ($F^{14}C \sim 1$). In contrast, CO₂ produced by thermogenic methane oxidation will have a fossil 517 $F^{14}C$ signature, because the methane originates from ancient organic rich sediments that contain no measurable radiocarbon 518 ($F^{14}C \sim 0$). While measuring methane concentrations quantitatively was not possible with our analytical setup, qualitative 519 data shows that methane concentrations in Milandre cave air and catchment borehole samples were exceedingly low (\sim 90 to 520 970 ppb), suggesting methane oxidation may occur in the Milandre subsurface environment. Methanotrophic bacteria have 521 been identified in 98 % of soils sampled from 21 North American caves at a mean bacterial abundance of 0.88 % (Webster

522 et al., 2022). Methanotrophic bacteria in caves significantly contribute to methane consumption, with a study in Pindal Cave 523 (NW Spain) showing how methanotrophic bacteria associated with moonmilk deposits remove 65 % to 90 % of atmospheric 524 methane entering the cave (Martin-Pozas et al., 2022). As our cave and borehole CO_2 samples have a $\delta^{13}C$ of \sim -26 % and a 525 variable $F^{14}C$ in the cave air and shallow meadow samples, we cannot rule out a contribution of methane oxidation from 526 biogenic processes actively occurring in Milandre. However, this would not explain the depleted radiocarbon signature that 527 we measured episodically in the cave air. Methane evolved abiogenically from pore fluids in Oxfordian marls may have an 528 isotopic ratio similar to that measured in our samples if thermogenically derived with a dominant conversion of CH_4 to CO_2 . 529 However, it is unlikely that this process occurred in the Milandre cave sediments given the lack of organic rich sedimentary 530 rocks in the stratigraphy. Thus, while we cannot quantify the importance of methane oxidation on the subsurface carbon 531 budget at our site, it is unlikely that methane oxidation processes are responsible for the variation in radiocarbon ages in cave 532 air CO_2 .

533

534 Despite the apparent limiting factors for microbial growth in caves, it is known that different organisms are able to thrive 535 within this niche including bacteria, archaea, algae, and fungi. In terms of bacteria, Proteobacteria is typically reported as the 536 dominant group in caves (Zhou et al., 2007; Tomczyk-Żak & Zielenkiewicz, 2016). However, in some cases Actinobacteria 537 is the largest group of microbes (Wiseschart et al., 2018). In two Chinese caves with high CO₂ concentrations (> 3,000 ppm), 538 Proteobacteria, Actinobacteria, Bacteroidetes, and Thaumarchaeota were the dominant phyla (Chen et al., 2023). Hundreds 539 of fungi taxa have been described in caves globally, with Ascomycota being the most commonly reported (Gherman et al., 540 2014). Though not yet thoroughly investigated, diverse communities of protists have also been identified within caves 541 (Gogoleva et al., 2024), as well as archaea (Biagioli et al., 2023), and algae (Kosznik- Kwaśnicka et al., 2022). As biological 542 processes generally favour the incorporation of lighter ¹²C compared to ¹³C, the respiration of these organisms would 543 contribute an organic signature (lower δ^{13} C and a F^{14} C corresponding to the age of the carbon source being consumed, which 544 can range from modern to more aged F¹⁴C) to the CO₂ composition of cave air at Milandre cave. With the isotopic analysis 545 used in this study, and because we did not analyse the microbial community diversity present in Milandre cave and its 546 catchment, the CO₂ contributions from different types of microbial processes cannot be distinguished from one another. We 547 are only able to distinguish between "organic" processes (in-cave microbial, soil, root, and fungi respiration) which produce 548 a CO₂ with a lower δ^{13} C signature and a range of F^{14} C depending on the age of the organic material consumed, and 549 "inorganic" processes (carbonate degassing and atmospheric ventilation) which contribute CO_2 with a higher $\delta^{13}C$ and a 550 range of F¹⁴C.

551

552 Varying contributions of host rock-derived carbon to cave air through shifts in the host rock dissolution regime can affect the isotopic composition of cave air. Dissolution of the host rock carbonate can occur under a wide range of conditions 554 between two extreme cases: completely closed and completely open systems. In a completely closed system, the aqueous 555 solution becomes isolated from the soil CO₂ reservoir after passing into the unsaturated zone resulting in a theoretical 50:50

556 contribution ratio of carbon ions in solution from the carbonate host rock and from soil air, and overall decreasing F¹⁴C to as 557 low as 0.5 (Fohlmeister et al., 2011; Milanolo & Gabrovšek, 2015). On the other hand, in a completely open system the 558 aqueous solution can continuously exchange with an unlimited soil CO₂ reservoir resulting in most carbon atoms sourced 559 from the soil CO₂ reservoir, and the rock contribution being minimal (Fohlmeister et al., 2011). Most natural systems exist in 560 an intermediate state between completely open and completely closed settings.

561

562 If the seasonal variability in CO_2 F¹⁴C in Milandre cave reflected seasonal shifts in the "openness" of the system, summers 563 (with higher F¹⁴C) would be characterised by a more open system with higher rates of exchange between the aqueous 564 solution and the soil CO_2 reservoir. The observed shift to lower F¹⁴C in winter would reflect a more closed system with a 565 higher contribution of the F¹⁴C free carbonate bedrock. Shifts in the open-closed continuum would likely result in changes in 566 the δ^{13} C of the endmember (Fairchild & Baker, 2012) which is not seen in the cave air, with an expected lower δ^{13} C in a 567 more open system, and an increase in a more closed system because of the higher carbonate host rock carbon contribution 568 (δ^{13} C ≈ 0 ‰). However, varying amounts of isotopic fractionation can occur when CO_2 is degassed from the drip water DIC 569 pool into the cave atmosphere, potentially influencing the isotopic composition of the measured cave air CO_2 (Mickler et al., 570 2019).

571

572 We constructed a mixing model which allows us to evaluate how much variability in the Keeling plot y-intercept (i.e. the 573 second source of carbon to cave air besides the atmosphere) can be explained by variation in DIC contribution from 574 dissolution regime changes and degassing fractionation. This model assumes that the Keeling plot y-intercept is itself a 575 mixture of two endmembers that contribute CO_2 to cave air, the modern soil $(F^{14}C_{soil} = 1)$, and the DIC $(F^{14}C_{DIC})$, where the 576 $F^{14}C_{DIC}$ represents a mixture of dissolved soil CO_2 and DIC from carbonate mineral dissolution, which we can constrain with 577 our measured DIC values. The $F^{14}C_{soil}$ represents direct input of CO_2 soil gas into the cave.

578

579 The mixing ratio between $F^{14}C_{soil}$ and $F^{14}C_{DIC}$ results in the $F^{14}C$ of CO_2 of the karst endmember ($F^{14}C_{cave}$). Thus, the cave 580 air CO_2 $F^{14}C$ can be expressed as (where f is fraction, defined as between 0 and 1):

581

$$F^{14}C_{cave} = f_{soil}F^{14}C_{soil} + f_{DIC}F^{14}C_{DIC}$$
 (3)

583

584 Since
$$f_{DIC} = 1 - f_{soil}$$
 :

586
$$F^{14}C_{cave} = f_{soil}F^{14}C_{soil} + (1 - f_{soil})F^{14}C_{DIC}$$
 (4)

```
587
```

588 For F¹⁴C, fractionation is generally negligible during carbonate dissolution and degassing compared to δ^{13} C, due to unit 589 conversion i.e. % vs % (Fohlmeister et al., 2011). We use the mixing calculation (Eq. 4) to estimate the contributions of f_{soil} 590 and f_{DIC} using the highest (0.94), an intermediate (0.90), and the lowest (0.88) measured cave CO₂ F¹⁴C values ($F^{14}C_{cave}$), 591 and F¹⁴C DIC ($F^{14}C_{DIC}$) based on the highest (0.98) intermediate (0.88) and lowest (0.78) measured values of drip water 592 DIC. We find that when $F^{14}C_{DIC} = 0.98$, the mixing model results in impossible scenarios with $f_{soil} > 1$ and $f_{DIC} < 0$ because 593 this value is higher than the highest $F^{14}C_{cave}$. When $F^{14}C_{DIC} = 0.88$ it results in a highly unlikely scenario based on our 594 observations and the literature where $f_{soil} = 0$ and $f_{DIC} = 1$, as this corresponds to the lowest $F^{14}C_{cave}$ value (Fig. 9a). Only 595 the scenario with lowest $F^{14}C_{DIC} = 0.78$ produced realistic mixing fractions. Overall, this implies that there is a discrepancy 596 between the measured $F^{14}C_{DIC} = 0.78$ produced realistic mixing fractions. Overall, this implies that there is a discrepancy 596 between the measured $F^{14}C_{DIC} = 0.78$ produced by a simplified mixing model based on the $F^{14}C$ of cave CO₂, with 597 $F^{14}C_{DIC}$ values too high to result in the $F^{14}C_{cave}$ composition that we observe. Thus, carbonate dissolution and subsequent 598 degassing of CO₂ from drip water DIC to cave air is unlikely to be the dominant process explaining the shifts in cave air $F^{14}C_{599}$ over time.

602 As our mixing ratios derived from measured DIC values were mostly not realistic according to the two endmember mixing 603 scenario, we considered how a wider theoretical range of $F^{14}C_{DIC}$ values (from closed to mainly open system dissolution 604 conditions, 0.50 to 0.90 F¹⁴C) would affect the contributing fractions of f_{soil} and f_{DIC} . Variations in $F^{14}C_{DIC}$: 0.50 to 0.85 605 result in viable mixing fractions across the range of $F^{14}C_{cave}$, with the f_{soil} (20 to 76 %) and f_{DIC} (24 to 80 %) differing 606 widely (Fig. 9b).

608 As the mean value of cave CO₂ δ^{13} C is -26 ‰ (we take a range from -25 to -27 ‰), we created a similar two-endmember 609 mixing calculation for δ^{13} C values to test whether the mixing ratios derived from F¹⁴C translate to observed δ^{13} C values. For 610 this we used the mean δ^{13} C of soil CO₂ ($\delta^{13}C_{soil}$) = -26 ‰, and the δ^{13} C of the DIC ($\delta^{13}C_{DIC}$) = -15 ‰ (estimated from a 611 mean of the δ^{13} C produced during the F¹⁴C DIC AMS measurement (see Appendix B)).

613 Fractionation effects during degassing must be considered when modelling δ^{13} C. If equilibrium fractionation between DIC 614 and $CO_{2(g)}$ occurs, the fractionation factor ($\Delta^{13}C_{HCO3-CO2,eq}$) at 10.5 °C between HCO₃- and CO₂ is 9.54 ‰, with the gas 615 being 9.54 ‰ depleted in ¹³C relative to the fluid (Mook et al., 1974). Kinetic fractionation can occur during rapid degassing 616 of CO_2 as well as during rapid precipitation of carbonate minerals (Mickler et al., 2019). If kinetic fractionation occurs 617 during degassing, this results in a greater depletion of the dissolved CO_2 in ¹³C compared to equilibrium fractionation (i.e. a 618 more positive $\delta^{13}C_{DIC}$). The possible ranges reported for the composition of CO_2 generated from kinetic fractionation during 619 degassing in caves vary widely, with some reporting $\Delta^{13}C_{HCO3-CO2,kin}$ close to that resulting from equilibrium fractionation 620 (Dulinski & Rozanski, 1990), and others a range of 10 to 65 ‰ (Mickler et al., 2019). The extent of kinetic fractionation is 621 expected to depend on the amount of degassing that occurs, which is a function of the disequilibrium between the fluid and 622 the surrounding air (Frisia et al., 2011). In our system with limited geochemical data regarding fluid compositions, it is 623 difficult to determine what extent of kinetic fractionation may have occurred. Hence, we first assume that the fractionation is 624 < -9.54 ‰ (i.e., greater compared to equilibrium conditions) and take a moderate but arbitrary value ballpark of 625 $\Delta^{13}C_{HCO3-CO2,kin} = 30$ ‰.

626

627 A mixing calculation is then applied to assess if the measured range of the karst endmember $\delta^{13}CO_2$ given by the Keeling 628 plot can be consistent with the extended range of $F^{14}C_{DIC}$ (0.50 to 0.85 $F^{14}C$) and measured $F^{14}C_{cave}$ under conditions with 629 equilibrium degassing and kinetic degassing:

630

631 Equilibrium degassing:

632
$$\delta^{13}C_{cave} = f_{soil}\delta^{13}C_{soil} + f_{DIC}(\delta^{13}C_{DIC} - \Delta^{13}C_{HCO3-CO2,eq})$$
 (5)

633

634 Kinetic degassing:

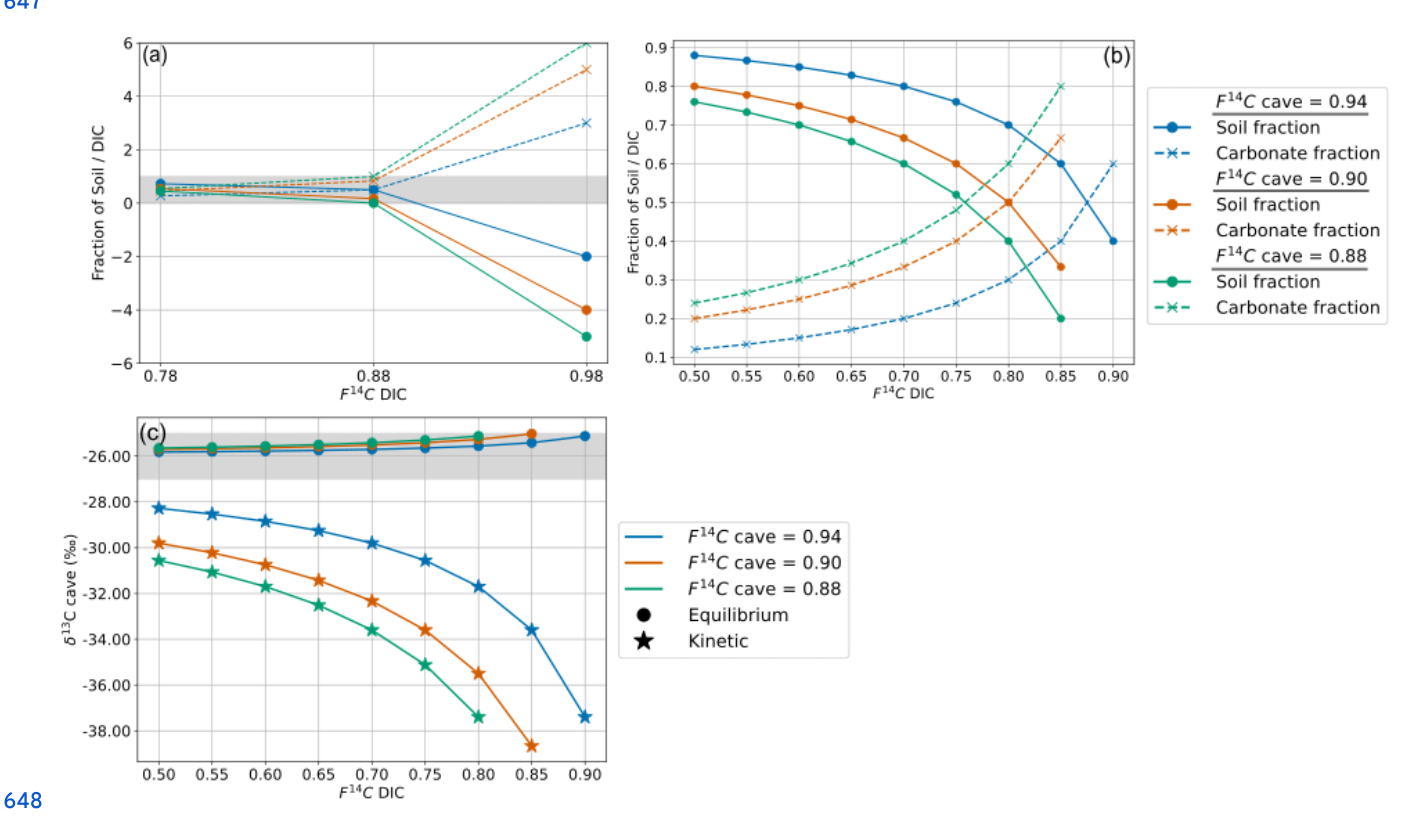
635
$$\delta^{13}C_{cave} = f_{soil}\delta^{13}C_{soil} + f_{DIC}(\delta^{13}C_{DIC} - \Delta^{13}C_{HCO3-CO2,kin})$$
 (6)

636

637 For the maximum (0.94), intermediate (0.90), and minimum (0.88) values of the endmember F¹⁴C, only equilibrium 638 fractionation during degassing can explain the observed $\delta^{13}C_{cave}$ value of approximately -26 ‰ (Fig. 9c). Kinetic 639 fractionation scenarios result in very negative $\delta^{13}C_{cave}$ values which do not fit those measured, except when using very small 640 kinetic fractionation factors similar to that of the equilibrium fractionation ($\Delta^{13}C_{HCO3-CO2,kin}$ of -10 ‰, see Appendix C). It 641 is possible that kinetic fractionation occurs between Milandre cave waters and the cave air due to atmospheric ventilation

642 which occurs year-round. The atmospheric air which enters from the upper entrance in the summer and the lower entrance in 643 the winter creates a concentration gradient between the CO₂ present within cave waters and the concentration in the cave 644 atmosphere. However, the rapidly increasing pCO₂ with distance from the cave entrance (Fig. 8a) implies that the 645 concentration gradients required for kinetic fractionation do not occur throughout most of the cave passage and that kinetic 646 influences are probably minimal.





649 Figure 9. a) Mixing model between f_{soil} and f_{DIC} for the measured range of F¹⁴C DIC values and F¹⁴C cave values of 0.94 (blue), 0.9 (orange) 0.88 (green). The grey bar shows physically possible mixing ratios between 0 and 1. b) Mixing model between f_{soil} and f_{DIC} 651 using the extended DIC F¹⁴C range and cave air F¹⁴C values. c) Cave air δ^{13} C for varying DIC F¹⁴C and cave air F¹⁴C values with 652 equilibrium fractionation at -9.54 % (circles) and kinetic fractionation at -30 % (stars). The grey bar shows cave air δ^{13} C range 653 which fits the measured values between -25 % and -27 %.

654

655 Overall, the $F^{14}C_{DIC}$ measured beyond $F^{14}C = 0.90$ is too high to reproduce our measured cave air CO_2 $F^{14}C$ and $\delta^{13}C$. The 656 $F^{14}C_{DIC}$ is based on the analysis of 9 drip water sites of varying drip rates and ecosystem coverage over the course of one 657 year. It is possible that the sampling set up did not capture the true range of $F^{14}C_{DIC}$ in the drip water, though this hypothesis

658 is highly unlikely due to the diversity in drip rate and hydrological response of drips measured, and we believe our DIC data 659 to be representative of the system.

660

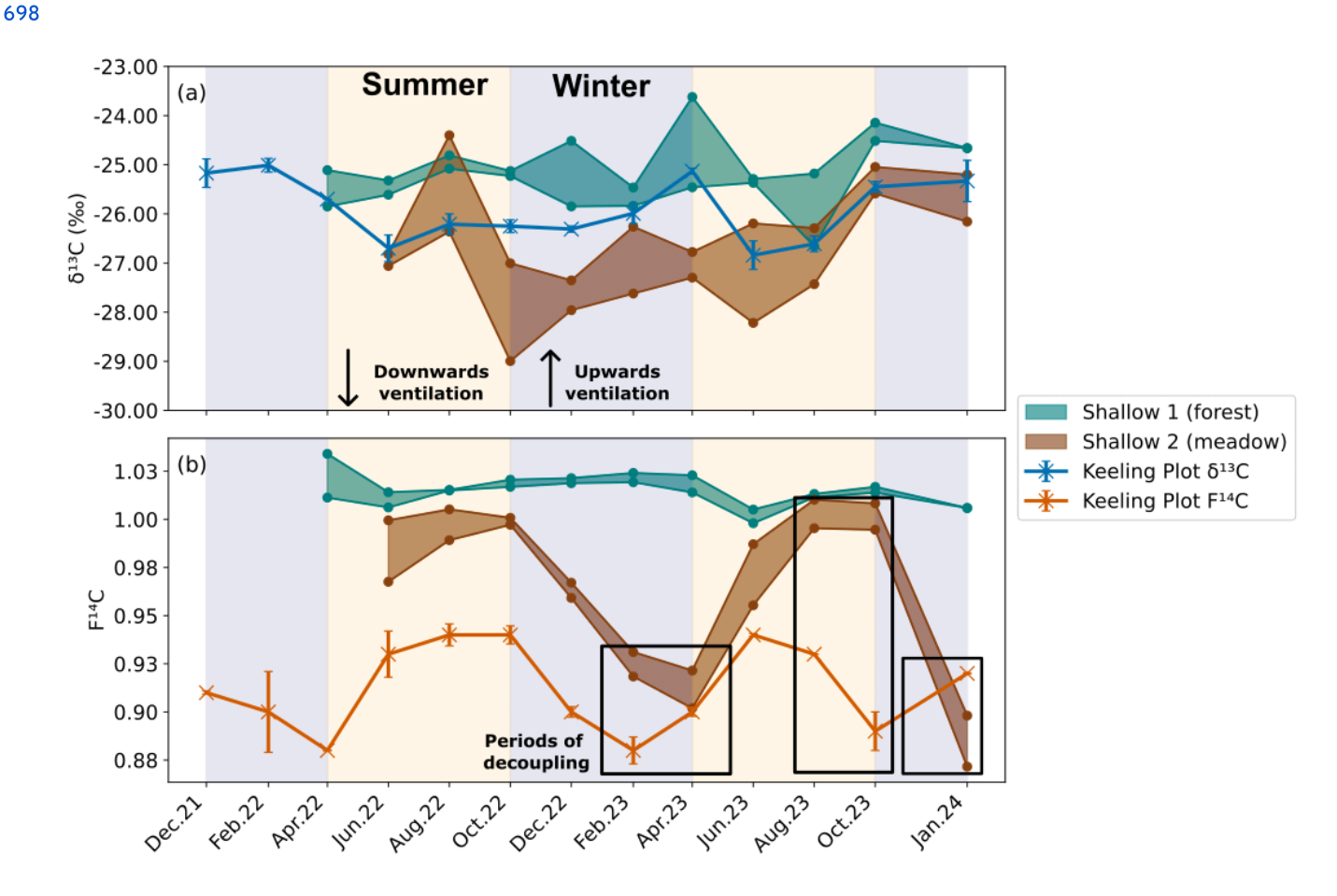
The $F^{14}C_{DIC}$ of the cave river was not measured, however previous studies investigating the Milandre cave river have suggested that in non-flooding conditions the river is fed by slow diffuse flow as the unsaturated zone acts as a buffer, storing water and dampening the signal of normal rainfall. During flooding events, the unsaturated zone aquifer is bypassed and the stream is mainly fed through fracture flow (Perrin et al., 2003; Savoy et al., 2011). A diffuse flow fed river is likely to have isotopic characteristics similar to that of the drip waters, which have higher $F^{14}C$ suggesting more open system dissolution conditions. In contrast, times of flooding and soil saturation result in less exchange with the soil gas reservoir, leading to dissolution under more closed conditions (Perrin et al., 2003; Savoy et al., 2011). However, the drip water $F^{14}C_{DIC}$ is relatively stable over one year of monitoring in a variety of hydrological conditions, implying that variations in host rock dissolution and degassing dynamics are not the explanation for the variation in $F^{14}C$ and $\delta^{13}C$ of the endmember.

670

671 The meadow soil boreholes in the doline (Shallow 2) have similar patterns in CO₂ composition to the karst endmember, with 672 a δ¹³C of -26 ‰ and variable F¹⁴C (Fig. 10a & b). In 2022, the F¹⁴C in the meadow soil and karst endmember align closely 673 over the seasonal cycle, but then decouple slightly in 2023 during the transitional periods between winter and spring where 674 the karst endmember F¹⁴C changes before the meadow. This suggests that, instead of the soils influencing the cave air due to 675 seasonal changes in soil respiration, the cave ventilation regime may be influencing the soil CO₂ F¹⁴C. The cave ventilates 676 upwards in winter from Downstream to Upstream in a chimney effect (and vice versa in summer). Here, the lower F¹⁴C karst 677 endmember CO₂ may flow upwards through the highly fractured unsaturated zone of the doline and ventilate the meadow 678 soils, resulting in a mixture of low F¹⁴C CO₂ from the karst endmember and modern CO₂ from the soils. This possibly reflects 679 a contribution of older CO₂ from within the karst itself, likely from a "ground air" reservoir of older respiring organic 680 material in the unsaturated zone as found by several other studies (Breecker et al., 2012; Noroha et al., 2015; Mattey et al., 681 2016; Bergel et al., 2017). It is possible that several reservoirs of older organic material exist throughout the downstream 682 catchment of Milandre which may contribute the low F¹⁴C CO₂ to the ventilating cave air in winter. In summer the 683 ventilation reverses, and the higher F¹⁴C CO₂ from the soil is transported downwards into the cave, increasing the F¹⁴C of the 684 cave endmember CO₂. The F¹⁴C of the karst endmember is always lower than the meadow soil F¹⁴C, implying that there is 685 always mixing between the soils and the karst endmember (which additionally also reflects the DIC contribution). Similar 686 upwards transport of CO₂ in karst boreholes has been observed in Nerja Cave, Spain (Benavente et al., 2010; Benavente et 687 al., 2015), and in the Gibraltar karst (Mattey et al., 2016). We do not observe significant effects of the winter upwards 688 ventilation in the F¹⁴C CO₂ in any of the deeper boreholes in the meadow or any of the boreholes in the forest. This could be 689 related to the location of Shallow 2 in the doline, whilst the rest of the boreholes are situated higher on the banks (Deep 3 and 690 Deep 4), or further away from the doline in the forest (Deep 1 and Deep 2). The topography difference between the higher 691 forest and lower meadow likely reflects influences of the secondary porosity in the bedrock, which is likely more highly 692 fractured in the meadow doline formation compared to the forest. As the doline structure likely has a higher secondary 693 porosity and is more highly fractured than the higher bedrock, ventilation effects may be more important here than at the 694 other locations.



699



700 Figure 10. Comparison between the a) δ^{13} C and b) F^{14} C of the shallow depth boreholes in the forest (Shallow 1, green) and meadow 701 (Shallow 2, brown), and the Keeling plot endmembers δ^{13} C (blue) and F^{14} C (orange) also show in Figure 7. Summer (yellow) and 702 winter (blue) seasons are highlighted by the coloured background. The direction of cave ventilation is shown by the arrows with 703 downwards ventilation (from Upstream to Downstream) in summer, and upwards ventilation (Downstream to Upstream). Periods 704 of decoupling between the F^{14} C of the meadow borehole and the cave endmember are shown in black boxes.

The accumulation of the older organic carbon in the unsaturated zone likely occurs over time. Soil layers in karst regions often accumulate on bedrock with deep vertical fractures (Cheng et al., 2023). This decreases the ability of long-term storage of older soil carbon pools due to preferential fracture flow, also known as subsurface leakage, which destabilises the oldest soil layer and leads to export of older carbon into the unsaturated zone (Sánchez-Cañete et al., 2018; Wan et al., 2018). Several studies have acknowledged this potential source of CO₂ produced autochthonously inside the unsaturated zone by the microbial degradation of this old soil, plant, or root material which was previously washed into the unsaturated zone, contributing older CO₂ to the ground air mix (Noronha et al., 2015; Bergel et al., 2017; Ding et al., 2023).

713 6 Conclusion

We conducted a comprehensive investigation over two years into the dynamics of CO_2 concentrations, $\delta^{13}C$ and $F^{14}C$ values 715 across different land covers and soil types within the Critical Zone at Milandre cave in northern Switzerland. Our analysis 716 found distinct seasonal fluctuations in CO_2 levels in soil boreholes in both forest and meadow areas, with higher 717 concentrations during summer compared to winter. Low $\delta^{13}C$ values of \sim -26 ‰ indicate respiration of C3 plants which 718 dominate the catchment area. The stable modern $F^{14}C$ of \sim 1.00 in shallow forest boreholes indicated a year-round modern 719 CO_2 contribution from tree and plant roots to the subsurface, consistent with a well-ventilated soil. On the other hand, 720 samples from meadow boreholes situated in a doline with a thick, well developed soil cover displayed seasonality in $F^{14}C$ 721 from \sim 0.88 in the winter and spring to \sim 1.00 in summer.

722

723 In the unsaturated zone we observed substantial variability in CO_2 concentrations across the catchment ($\sim 3,000$ to $\sim 37,000$ 724 ppmV), with higher concentrations in boreholes with forest cover than those with meadow cover. Despite differences in 725 surface vegetation, the isotopic compositions of $\delta^{13}C$ and $F^{14}C$ remained stable in both forest and meadow environments, 726 reflecting the dominant modern C3 vegetation signature contributing to the ground air. The year-round modern unsaturated 727 zone CO_2 in meadow boreholes Deep 3 and Deep 4 contrasts with the seasonally attenuated signal in the thicker meadow 728 soils.

729

Table 1.25 Large variations in cave air CO_2 concentrations (atmospheric to ~ 30,000 ppmV), $\delta^{13}C$ (~ -9 to -25 ‰), and $F^{14}C$ (0.88 to 731 0.98), are controlled by seasonal temperature-driven cave ventilation. The seasonal changes in the isotopic composition of 732 the Keeling plot derived karst endmember cannot be explained with the observed DIC $F^{14}C$ range, suggesting that bedrock 733 dissolution and degassing dynamics are likely not the cause of the isotopic variation in the cave air. The isotopic 734 characteristics of the cave air are comparable to those of the meadow doline soil. The seasonal variability in karst 735 endmember CO_2 $F^{14}C$ precedes that in the soil, and is always older. This suggests that cave ventilation contributes older CO_2 736 to the doline soils, likely sourced from a reservoir of aged organic material in the unsaturated zone, during the upward winter

737 ventilation regime. In summer, the reversed downwards ventilation contributes younger soil CO₂ to the cave, mixing with the

738 older unsaturated zone reservoir.

739

740 Our study provides important insights into how carbon is transported to the subsurface in karstic Critical Zones.

741 Understanding these processes is crucial for accurate estimation of the size of subsurface CO2 pools (ground air), and to

742 refine terrestrial CO₂ budgets. Moving forward, it would be beneficial to undertake more detailed investigation of CO₂

743 transport into the subsurface implementing ¹⁴C analysis to further constrain the sources of ground air. Furthermore, higher

744 resolution monitoring over periods of interest, could assist us in understanding short-term variations.

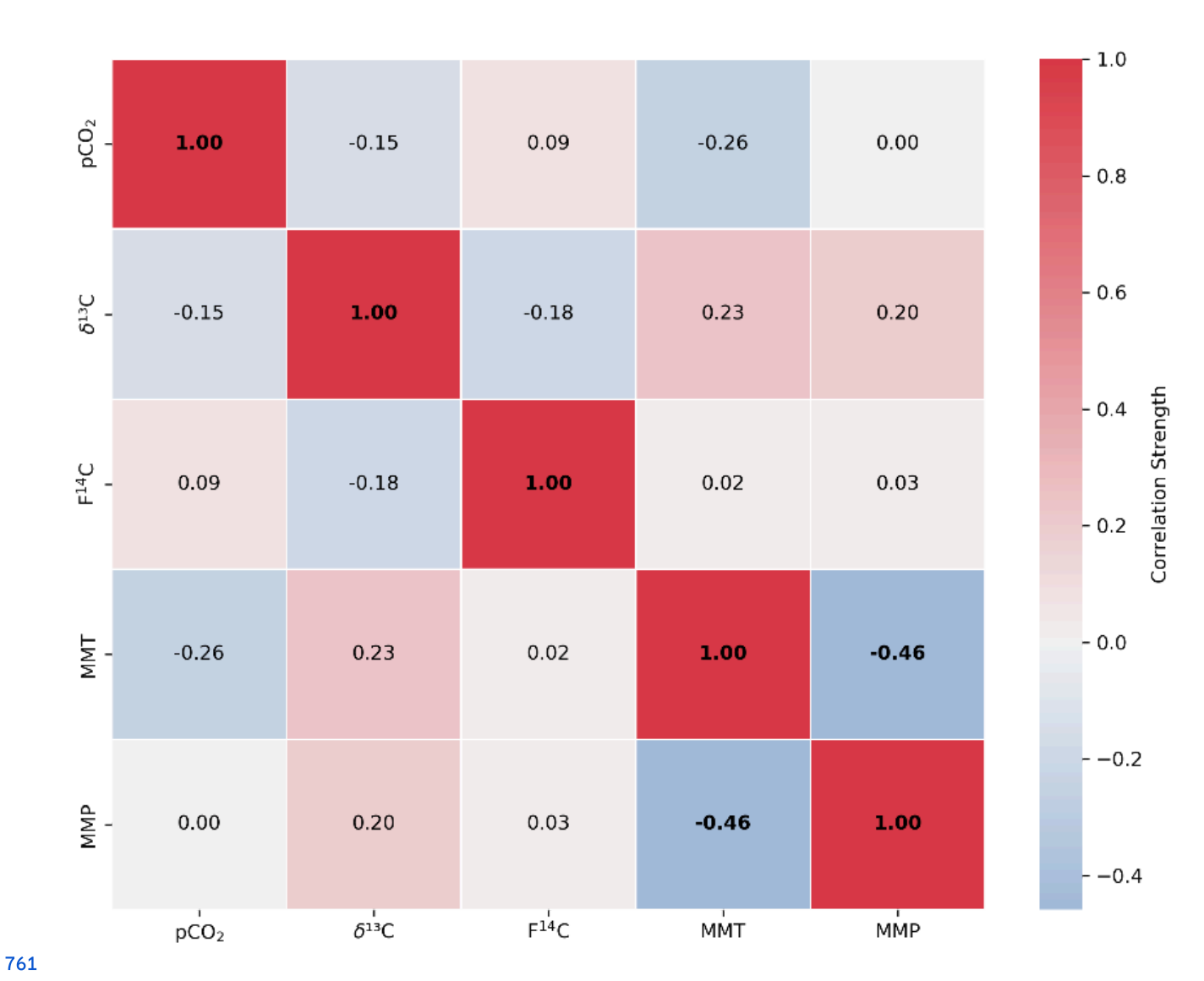
745 Appendix A



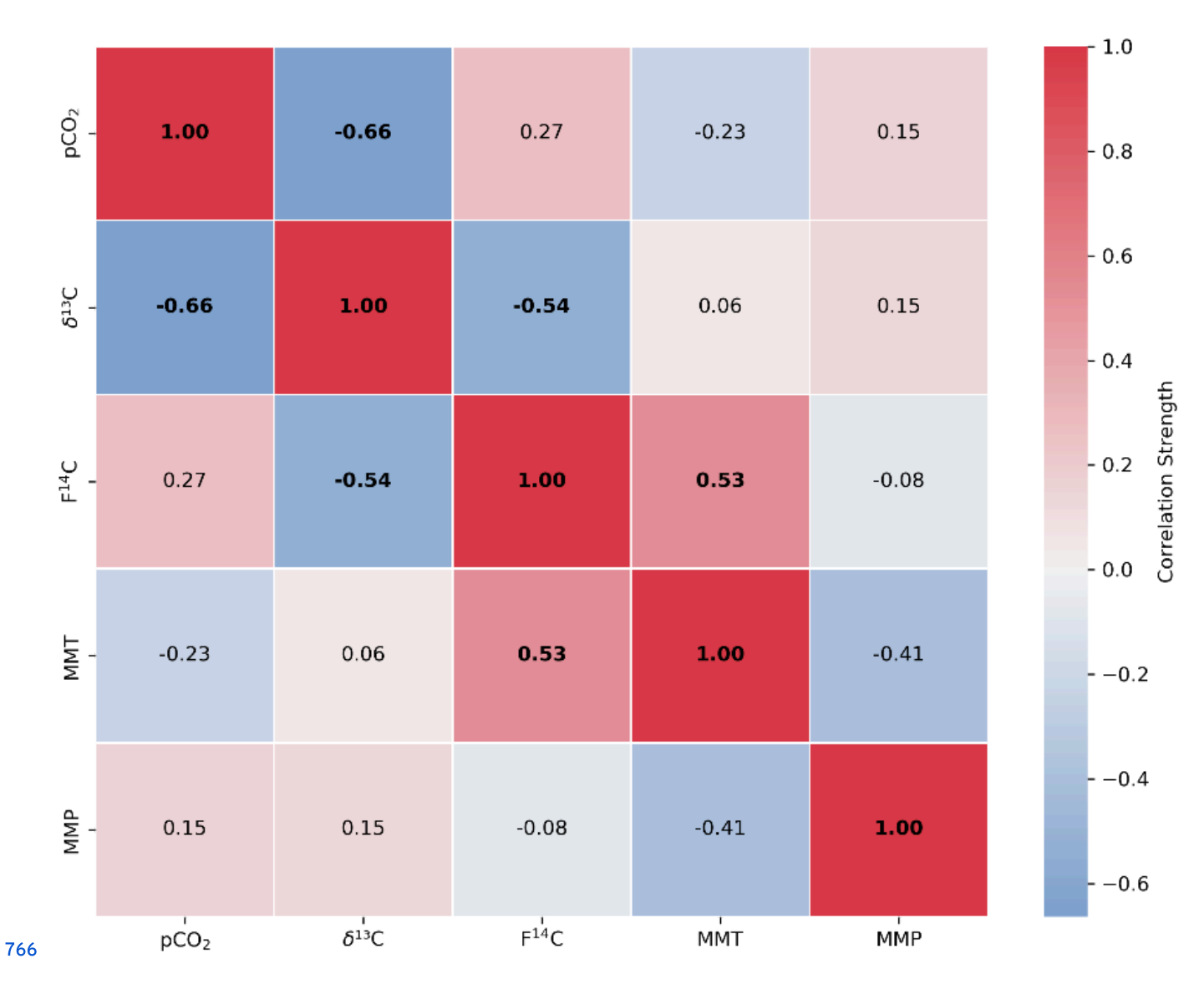
748 A1 Spearman's rank correlation matrix displaying the Spearman's rho of CO_2 concentration, $\delta^{13}C$ and $F^{14}C$, Mean Monthly 749 Temperature (MMT) and Mean Monthly Precipitation (MMP) from Fahy weather station from samples from soil depth boreholes 750 Shallow 1. Parameters with a significant correlation (positive or negative) are bolded and the strength of the correlation is 751 indicated by the blue – red colour bar.



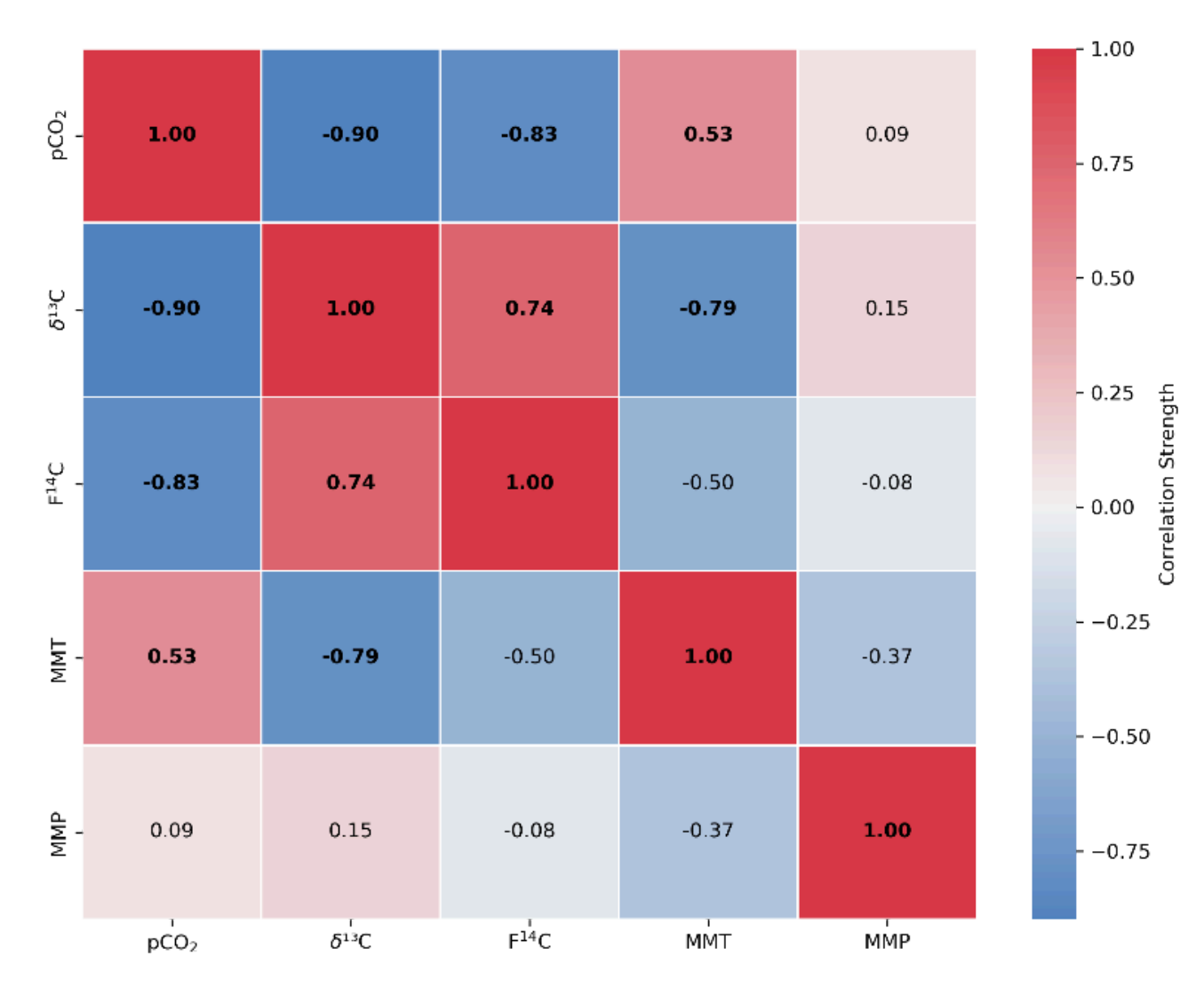
756 A2 Spearman's rank correlation matrix displaying the Spearman's rho of CO_2 concentration, $\delta^{13}C$ and $F^{14}C$, Mean Monthly 757 Temperature (MMT) and Mean Monthly Precipitation (MMP) from Fahy weather station from samples from soil depth borehole 758 Shallow 2. Parameters with a significant correlation (positive or negative) are bolded and the strength of the correlation is 759 indicated by the blue – red colour bar.



762 A3 Spearman's rank correlation matrix displaying the Spearman's rho of CO_2 concentration, $\delta^{13}C$ and $F^{14}C$, Mean Monthly 763 Temperature (MMT) and Mean Monthly Precipitation (MMP) from Fahy weather station from samples from unsaturated zone 764 depth boreholes Deep 1 and Deep 2. Parameters with a significant correlation (positive or negative) are bolded and the strength of 765 the correlation is indicated by the blue – red colour bar.



767 A4 Spearman's rank correlation matrix displaying the Spearman's rho of CO_2 concentration, $\delta^{13}C$ and $F^{14}C$, Mean Monthly 768 Temperature (MMT) and Mean Monthly Precipitation (MMP) from Fahy weather station from samples from unsaturated zone 769 depth boreholes Deep 3 and Deep 4. Parameters with a significant correlation (positive or negative) are bolded and the strength of 770 the correlation is indicated by the blue – red colour bar.



778 A5 Spearman's rank correlation matrix displaying the Spearman's rho of CO_2 concentration, $\delta^{13}C$ and $F^{14}C$, Mean Monthly 779 Temperature (MMT) and Mean Monthly Precipitation (MMP) from Fahy weather station from samples from the Downstream 780 cave site. Parameters with a significant correlation (positive or negative) are bolded and the strength of the correlation is indicated 781 by the blue – red colour bar

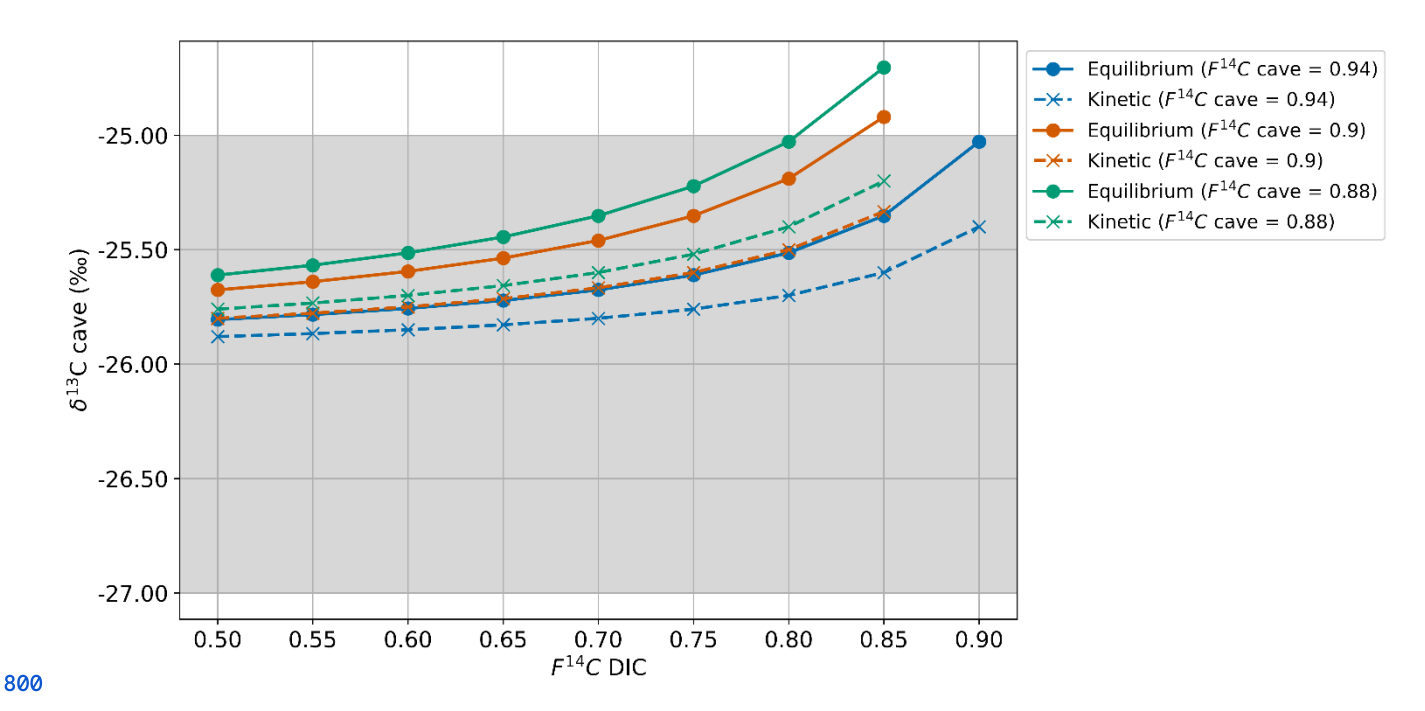


783 A6 Spearman's rank correlation matrix displaying the Spearman's rho of CO_2 concentration, $\delta^{13}C$ and $F^{14}C$, Mean Monthly 784 Temperature (MMT) and Mean Monthly Precipitation (MMP) from Fahy weather station from samples from the Upstream cave 785 stie. Parameters with a significant correlation (positive or negative) are bolded and the strength of the correlation is indicated by 786 the blue – red colour bar.

793 B1 Drip water dissolved inorganic carbon $F^{14}C$ and AMS derived $\delta^{13}C$ from the actively dripping galleries nearby Upstream and 794 Downstream.

		F ¹⁴		
Drip	Sampling date	C	F¹4C % error	AMS δ^{13} C (%)
GF1	Dec.21	0.86	0.92	-13.6
GF2	Dec.21	0.94	0.91	-14.3
GR2	Dec.21	0.91	0.92	-12.4
GR3	Dec.21	0.98	0.93	-13.5
GR4	Dec.21	0.91	0.97	-14.7
GR5	Dec.21	0.90	0.97	-14.2
GR6	Dec.21	0.85	1.02	-13.6
GF1	Feb.22	0.87	0.99	-12.6
GF3	Feb.22	0.95	0.96	-12.7
GR3	Feb.22	0.90	0.97	-14.1
GR4	Feb.22	0.89	0.99	-12.7
GR6	Feb.22	0.84	1.00	-11.9
GR6	Feb.22	0.88	0.99	-10.6
GF1	Apr.22	0.88	0.93	-12.8
GF2	Apr.22	0.93	0.89	-11.6
GF3	Apr.22	0.98	0.86	-12.1
GR1	Apr.22	0.87	0.90	-12.6
GR2	Apr.22	0.89	0.92	-12.1
GR3	Apr.22	0.90	0.93	-12.2
GR4	Apr.22	0.90	0.93	-13.4
GR5	Apr.22	0.89	0.98	-13.7
GR6	Apr.22	0.90	0.99	-13.6
GF1	Jun.22	0.87	1.11	-18.0
GF2	Jun.22	0.93	1.11	-18.9
GF3	Jun.22	0.96	1.07	-18.6
GR1	Jun.22	0.88	1.12	-17.4
GR2	Jun.22	0.93	1.09	-17.6
GR3	Jun.22	0.89	1.12	-17.9
GR4	Jun.22	0.89	1.12	-18.9
GR5	Jun.22	0.90	1.11	-17.9
GR6	Jun.22	0.92	1.12	-19.0
GF1	Aug.22	0.86	1.10	-17.1
GF2	Aug.22	0.92	1.12	-19.8

GR1	Aug.22	0.87	1.03	-8.9
GR2	Aug.22	0.91	1.09	-18.3
GR4	Aug.22	0.93	1.10	-19.2
GR5	Aug.22	0.91	1.10	-19.5
GR6	Aug.22	0.93	1.11	-20.8
GF1	Oct.22	0.84	1.05	-9.4
GF2	Oct.22	0.94	1.12	-20.3
GF3	Oct.22	0.95	1.11	-20.8
GR1	Oct.22	0.86	1.14	-17.2
GR2	Oct.22	0.88	1.14	-22.6
GR4	Oct.22	0.91	1.13	-18.7
GR5	Oct.22	0.89	1.13	-18.3
GR6	Oct.22	0.91	1.11	-19.1
GF1	Dec.22	0.86	1.01	-14.1
GF2	Dec.22	0.88	0.94	-14.1
GF3	Dec.22	0.94	0.95	-11.1
GR1	Dec.22	0.86	1.00	-11.5
GR4	Dec.22	0.89	0.98	-11.5
GR5	Dec.22	0.89	1.01	-12.6
GR6	Dec.22	0.78	1.02	-12.9



801 C1 Cave air δ^{13} C for varying DIC F¹⁴C and cave air F¹⁴C values with equilibrium fractionation at -9.54 ‰ (solid lines) and kinetic 802 fractionation at -10 ‰ (dashed lines).

804 Code and data availability

803

805 The data, code for Spearman's rank statistics, and code to reproduce the model results are publicly available on Zenodo at 806 https://doi.org/10.5281/zenodo.14253707.

807 Author contributions

- 808 Sarah Rowan: Conceptualization, Formal analysis, Investigation, Methodology, Visualization, Software, Writing original 809 draft preparation.
- 810 Marc Luetscher: Conceptualization, Resources, Visualization, Writing review & editing.
- 811 Thomas Laemmel: Methodology, Validation, Writing review & editing.
- 812 Anna Harris: Methodology, Writing review & editing.
- 813 Sönke Szidat: Writing review & editing.
- 814 Franziska Lechleitner: Conceptualization, Funding acquisition, Project administration, Resources, Supervision, Writing -
- 815 review & editing.

816 Competing interests

817 The authors declare that they have no conflict of interest.

818 Disclaimer

819

820 Acknowledgements

- 821 This work was supported by the Swiss National Science Foundation Ambizione grant number 186135. We gratefully thank
- 822 the staff of the Swiss Institute of Speleology and Karst Studies for their previous and continued work in Milandre cave, and
- 823 for their contribution of field assistance and expertise in karst science. Special thanks to Claudio Pastore for his assistance
- 824 during the through trip. We express our gratitude to the Spéléo Club Jura for the initial exploration of Milandre cave, and for
- 825 their persistent work and maintenance of the area. We also appreciate Daniel Pape, for continued access to the cave entrance
- 826 and boreholes. Thank you also to Madalina Jaggi, Dr. Oliver Kost, and Prof. Heather Stoll for providing access and support
- 827 using the Picarro system. Graphitizations and AMS measurements were also assisted by Michael Staub and Dr. Gary Salazar.
- 828 Generative AI (ChatGPT versions 3.5, 4 and 4o) was used for code troubleshooting.

829 References

- 830 Affolter, S., Steinmann, P., Aemisegger, F., Purtschert, R., & Leuenberger, M. (2020). Origin and percolation times of
- 831 Milandre Cave drip water determined by tritium time series and beryllium-7 data from Switzerland. Journal of
- 832 Environmental Radioactivity, 222, 106346. https://doi.org/10.1016/j.jenvrad.2020.106346

833

- 834 Atkin, O. K., Sherlock, D., Fitter, A. H., Jarvis, S., Hughes, J. K., Campbell, C., Hurry, V., & Hodge, A. (2009). Temperature
- 835 dependence of respiration in roots colonized by arbuscular mycorrhizal fungi. New Phytologist, 182(1), 188–199.
- 836 https://doi.org/10.1111/j.1469-8137.2008.02727.x

837

- 838 Atkinson, T. C. (1977). Carbon dioxide in the atmosphere of the unsaturated zone: An important control of groundwater
- 839 hardness in limestones. Journal of Hydrology, 35(1), 111–123. https://doi.org/10.1016/0022-1694(77)90080-4

840

- 841 Baldini, J. U. L., Bertram, R. A., & Ridley, H. E. (2018). Ground air: A first approximation of the Earth's second largest
- 842 reservoir of carbon dioxide gas. Science of The Total Environment, 616-617, 1007-1013.
- 843 https://doi.org/10.1016/j.scitotenv.2017.10.218

- 845 Benavente, J., Vadillo, I., Carrasco, F., Soler, A., Liñán, C., & Moral, F. (2010). Air Carbon Dioxide Contents in the Vadose
- 846 Zone of a Mediterranean Karst, Vadose Zone Journal, 9(1), 126–136, https://doi.org/10.2136/vzi2009.0027

- 848 Benavente, J., Vadillo, I., Liñán, C., del Rosal, Y., & Carrasco, F. (2015). Influence of the ventilation of a karst show cave on
- 849 the surrounding vadose CO2 reservoir (Nerja, South Spain). Environmental Earth Sciences, 74(12), 7731-7740.
- 850 https://doi.org/10.1007/s12665-015-4709-8

851

- 852 Bergel, S. J., Carlson, P. E., Larson, T. E., Wood, C. T., Johnson, K. R., Banner, J. L., & Breecker, D. O. (2017). Constraining
- 853 the subsoil carbon source to cave-air CO2 and speleothem calcite in central Texas. Geochimica et Cosmochimica Acta, 217,
- 854 112–127. https://doi.org/10.1016/j.gca.2017.08.017

855

- 856 Biagioli, F., Coleine, C., Piano, E., Nicolosi, G., Poli, A., Prigione, V., Zanellati, A., Varese, C., Isaia, M., & Selbmann, L.
- 857 (2023). Microbial diversity and proxy species for human impact in Italian karst caves. Scientific Reports, 13(1), 689.
- 858 https://doi.org/10.1038/s41598-022-26511-5

859

- 860 Billings, S., Richter, D., & Yarie, J. (1998). Soil carbon dioxide fluxes and profile concentrations in two boreal forests.
- 861 Canadian Journal of Forest Research, 28. https://doi.org/10.1139/cjfr-28-12-1773

862

- 863 Boyno, G., Yerli, C., Çakmakci, T., Sahin, U., & Demir, S. (2024). The effect of arbuscular mycorrhizal fungi on carbon
- 864 dioxide (CO2) emission from turfgrass soil under different irrigation intervals. Journal of Water and Climate Change, 15(2),
- 865 541–553. https://doi.org/10.2166/wcc.2024.482

866

- 867 Brantley, S. L., Goldhaber, M. B., & Vala, R. K. (2007). Crossing disciplines and scales to understand the critical zone.
- 868 Elements (Vol. 3, Issue 5, p. 8). https://doi.org/10.2113/gselements.3.5.307

869

- 870 Breecker, D. O. (2017). Atmospheric pCO2 control on speleothem stable carbon isotope compositions. Earth and Planetary
- 871 Science Letters, 458, 58–68. https://doi.org/10.1016/j.epsl.2016.10.042

872

- 873 Breecker, D. O., Payne, A. E., Quade, J., Banner, J. L., Ball, C. E., Meyer, K. W., & Cowan, B. D. (2012). The sources and
- 874 sinks of CO2 in caves under mixed woodland and grassland vegetation. Geochimica et Cosmochimica Acta, 96, 230–246.
- 875 https://doi.org/10.1016/j.gca.2012.08.023

- 877 Buzjak, N., Gabrovšek, F., Perşoiu, A., Pennos, C., Paar, D., & Bočić, N. (2024). CO2 Emission from Caves by
- 878 Temperature-Driven Air Circulation—Insights from Samograd Cave, Croatia. Climate, 12(12), Article 12.
- 879 https://doi.org/10.3390/cli12120199

- 881 Campeau, A., Bishop, K., Amvrosiadi, N., Billett, M. F., Garnett, M. H., Laudon, H., Öquist, M. G., & Wallin, M. B. (2019).
- 882 Current forest carbon fixation fuels stream CO2 emissions. Nature Communications, 10(1), Article 1.
- 883 https://doi.org/10.1038/s41467-019-09922-3

884

- 885 Chen, J., Li, Q., He, Q., Schröder, H. C., Lu, Z., & Yuan, D. (2023). Influence of CO2/HCO3- on Microbial Communities in
- 886 Two Karst Caves with High CO2. Journal of Earth Science, 34(1), 145 155. https://doi.org/10.1007/s12583-020-1368-9

887

- 888 Cheng, K., Liu, Z., Xiong, K., He, Q., Li, Y., Cai, L., & Chen, Y. (2023). Migration of Dissolved Organic Matter in the
- 889 Epikarst Fissured Soil of South China Karst. Land, 12(4), Article 4. https://doi.org/10.3390/land12040887

890

- 891 Chiodini, G., Caliro, S., Cardellini, C., Avino, R., Granieri, D., & Schmidt, A. (2008). Carbon isotopic composition of soil
- 892 CO2 efflux, a powerful method to discriminate different sources feeding soil CO2 degassing in volcanic-hydrothermal areas.
- 893 Earth and Planetary Science Letters, 274(3), 372–379. https://doi.org/10.1016/j.epsl.2008.07.051

894

- 895 Chiti, T., Neubert, R., Janssens, I., Curiel Yuste, J., Sirignano, C., & Certini, G. (2011). Radiocarbon based assessment of soil
- 896 organic matter contribution to soil respiration in a pine stand of the Campine region, Belgium. Plant and Soil, 344, 273–282.
- 897 https://doi.org/10.1007/s11104-011-0745-7

898

- 899 Diao, H., Wang, A., Yuan, F., Guan, D., & Wu, J. (2022). Autotrophic respiration modulates the carbon isotope composition
- 900 of soil respiration in a mixed forest. Science of The Total Environment, 807, 150834.
- 901 https://doi.org/10.1016/j.scitotenv.2021.150834

902

- 903 Ding, Y., Wang, D., Zhao, G., Chen, S., Sun, T., Sun, H., Wu, C., Li, Y., Yu, Z., Li, Y., & Chen, Z. (2023). The contribution
- 904 of wetland plant litter to soil carbon pool: Decomposition rates and priming effects. Environmental Research, 224, 115575.
- 905 https://doi.org/10.1016/j.envres.2023.115575

906

- 907 Dulinski, M., & Rozanski, K. (1990). 'Formation of 13C/12C Isotope Ratios in Speleothems: A Semi-Dynamic Model'.
- 908 Radiocarbon, 32(1), 7–16. https://doi.org/10.1017/S0033822200039904

- 910 Fairchild, I. J., & Baker, A. (2012). Speleothem Science: From Process to Past Environments. John Wiley & Sons.
- 911 https://doi.org/10.1002/9781444361094.ch5

- 913 Fohlmeister, J., Scholz, D., Kromer, B., & Mangini, A. (2011). Modelling carbon isotopes of carbonates in cave drip water.
- 914 Geochimica et Cosmochimica Acta, 75(18), 5219–5228. https://doi.org/10.1016/j.gca.2011.06.023

915

- 916 Frieling, J., Svensen, H. H., Planke, S., Cramwinckel, M. J., Selnes, H., & Sluijs, A. (2016). Thermogenic methane release as
- 917 a cause for the long duration of the PETM. Proceedings of the National Academy of Sciences, 113(43), 12059–12064.
- 918 https://doi.org/10.1073/pnas.1603348113

919

- 920 Frisia, S., Fairchild, I. J., Fohlmeister, J., Miorandi, R., Spötl, C., & Borsato, A. (2011). Carbon mass-balance modelling and
- 921 carbon isotope exchange processes in dynamic caves. Geochimica et Cosmochimica Acta, 75(2), 380-400.
- 922 https://doi.org/10.1016/j.gca.2010.10.021

923

- 924 Fitter, A. H., Heinemeyer, A., & Staddon, P. L. (2000). The impact of elevated CO2 and global climate change on arbuscular
- 925 mycorrhizas: A mycocentric approach. New *Phytologist*, 147(1), 179–187.
- 926 https://doi.org/10.1046/j.1469-8137.2000.00680.x

927

- 928 Garagnon, J., Luetscher, M., & Weber, E. (2022, July 1). Ventilation regime in a karstic system (Milandre Cave,
- 929 Switzerland). Conference: 18th International Congress of Speleology, Savoie Mont Blanc.

930

- 931 Gherman, V. D., Boboescu, I. Z., Pap, B., Kondorosi, É., Gherman, G., & Maróti, G. (2014). An Acidophilic
- 932 Bacterial-Archaeal-Fungal Ecosystem Linked to Formation of Ferruginous Crusts and Stalactites. Geomicrobiology Journal,
- 933 31(5), 407–418. https://doi.org/10.1080/01490451.2013.836580

934

- 935 Gigon, R. and Wenger, R. (1986): Inventaire spe'le 'ologique de la Suisse, canton du Jura. La Chaux-de-Fonds: Commission
- 936 Spéléologie de la Société helvétique des sciences naturelles.

937

- 938 Girault, F., Adhikari, L. B., France-Lanord, C., Agrinier, P., Koirala, B. P., Bhattarai, M., Mahat, S. S., Groppo, C., Rolfo, F.,
- 939 Bollinger, L., & Perrier, F. (2018). Persistent CO2 emissions and hydrothermal unrest following the 2015 earthquake in
- 940 Nepal. Nature Communications, 9(1), 2956. https://doi.org/10.1038/s41467-018-05138-z

- 942 Gogoleva, N. E., Nasyrova, M. A., Balkin, A. S., Chervyatsova, O. Y., Kuzmina, L. Y., Shagimardanova, E. I., Gogolev, Y.
- 943 V., & Plotnikov, A. O. (2024). Flourishing in Darkness: Protist Communities of Water Sites in Shulgan-Tash Cave (Southern
- 944 Urals, Russia). *Diversity*, 16(9), Article 9. https://doi.org/10.3390/d16090526

- 946 Hasenmueller, E. A., Gu, X., Weitzman, J. N., Adams, T. S., Stinchcomb, G. E., Eissenstat, D. M., Drohan, P. J., Brantley, S.
- 947 L., & Kaye, J. P. (2017). Weathering of rock to regolith: The activity of deep roots in bedrock fractures. Geoderma, 300,
- 948 11–31. https://doi.org/10.1016/j.geoderma.2017.03.020

949

- 950 Hashimoto, S., & Komatsu, H. (2006). Relationships between soil CO2 concentration and CO2 production, temperature,
- 951 water content, and gas diffusivity: Implications for field studies through sensitivity analyses. Journal of Forest Research,
- 952 11(1), 41–50. https://doi.org/10.1007/s10310-005-0185-4

953

- 954 Jeannin, P.-Y. (1998). Structure et comportement hydraulique des aquifères karstiques, [Unpublished doctoral dissertation],
- 955 University of Neuchâtel.

956

- 957 Jeannin, P.-Y., Hessenauer, M., Malard, A., & Chapuis, V. (2016). Impact of global change on karst groundwater
- 958 mineralization in the Jura Mountains. Science of The Total Environment, 541, 1208–1221.
- 959 https://doi.org/10.1016/j.scitotenv.2015.10.008

960

- 961 Kähkönen, M., Wittmann, C., Kurola, J., Ilvesniemi, H., & Salkinoja-Salonen, M. (2001). Microbial activity of boreal forest
- 962 soil in a cold climate. Boreal Environment Research, 6, 19–28.

963

- 964 Keeling, C. D. (1961). The concentration and isotopic abundances of carbon dioxide in rural and marine air. Geochimica et
- 965 Cosmochimica Acta, 24(3), 277–298. https://doi.org/10.1016/0016-7037(61)90023-0

966

- 967 Keller, C. K. (2019). Carbon Exports from Terrestrial Ecosystems: A Critical-Zone Framework. *Ecosystems*, 22(8),
- 968 1691–1705. https://doi.org/10.1007/s10021-019-00375-9

969

- 970 Kiers, E. T., Duhamel, M., Beesetty, Y., Mensah, J. A., Franken, O., Verbruggen, E., Fellbaum, C. R., Kowalchuk, G. A.,
- 971 Hart, M. M., Bago, A., Palmer, T. M., West, S. A., Vandenkoornhuyse, P., Jansa, J., & Bücking, H. (2011). Reciprocal
- 972 Rewards Stabilize Cooperation in the Mycorrhizal Symbiosis. Science, 333(6044), 880-882.
- 973 https://doi.org/10.1126/science.1208473

- 975 Kokoska, S., & Zwillinger, D. (2000). CRC Standard Probability and Statistics Tables and Formulae, Student Edition. CRC
- 976 Press.
- 977
- 978 Kosznik-Kwaśnicka, K., Golec, P., Jaroszewicz, W., Lubomska, D., & Piechowicz, L. (2022). Into the Unknown: Microbial
- 979 Communities in Caves, Their Role, and Potential Use. *Microorganisms*, 10(2), Article 2.
- 980 https://doi.org/10.3390/microorganisms10020222
- 981
- 982 Kottek, M., Grieser, J., Beck, C., Rudolf, B., & Rubel, F. (2006). World Map of the Köppen-Geiger Climate Classification
- 983 Updated. Meteorologische Zeitschrift, 15, 259–263. https://doi.org/10.1127/0941-2948/2006/0130
- 984
- 985 Kukuljan, L., Gabrovšek, F., Covington, M. D., & Johnston, V. E. (2021). CO2 dynamics and heterogeneity in a cave
- 986 atmosphere: Role of ventilation patterns and airflow pathways. Theoretical and Applied Climatology, 146(1), 91–109.
- 987 https://doi.org/10.1007/s00704-021-03722-w
- 988
- 989 Lekberg, Y., & Koide, R. T. (2008). Effect of soil moisture and temperature during fallow on survival of contrasting isolates
- 990 of arbuscular mycorrhizal fungi. Botany, 86(10), 1117–1124. https://doi.org/10.1139/B08-077
- 991
- 992 Li, Y., Yang, Y., Wang, X., Luo, W., Zhao, J., Sun, Z., Ye, Z., Chen, X., Shi, X., Xu, Y., & Baker, J. L. (2024). Sources and
- 993 transport of CO2 in the karst system of Jiguan Cave, Funiu Mountains, China. Science of The Total Environment, 918,
- 994 170507. https://doi.org/10.1016/j.scitotenv.2024.170507
- 995
- 996 Martin-Pozas, T., Cuezva, S., Fernandez-Cortes, A., Cañaveras, J. C., Benavente, D., Jurado, V., Saiz-Jimenez, C., Janssens,
- 997 I., Seijas, N., & Sanchez-Moral, S. (2022). Role of subterranean microbiota in the carbon cycle and greenhouse gas
- 998 dynamics. Science of The Total Environment, 831, 154921. https://doi.org/10.1016/j.scitotenv.2022.154921
- 999
- 1000 Mattey, D. P., Atkinson, T. C., Barker, J. A., Fisher, R., Latin, J.-P., Durrell, R., & Ainsworth, M. (2016). Carbon dioxide,
- 1001 ground air and carbon cycling in Gibraltar karst. Geochimica et Cosmochimica Acta, 184, 88-113.
- 1002 https://doi.org/10.1016/j.gca.2016.01.041
- 1003
- 1004 McDonough, L. K., Iverach, C. P., Beckmann, S., Manefield, M., Rau, G. C., Baker, A., & Kelly, B. F. J. (2016). Spatial
- 1005 variability of cave-air carbon dioxide and methane concentrations and isotopic compositions in a semi-arid karst
- 1006 environment. Environmental Earth Sciences, 75(8), 700. https://doi.org/10.1007/s12665-016-5497-5
- 1007

- 1008 MeteoSwiss. Retrieved 26 August 2024, from https://www.meteoswiss.admin.ch/
- 1009
- 1010 Mickler, P. J., Carlson, P., Banner, J. L., Breecker, D. O., Stern, L., & Guilfoyle, A. (2019). Quantifying carbon isotope
- 1011 disequilibrium during in-cave evolution of drip water along discreet flow paths. Geochimica et Cosmochimica Acta, 244,
- 1012 182–196. https://doi.org/10.1016/j.gca.2018.09.027
- 1013
- 1014 Milanolo, S., & Gabrovšek, F. (2015). Estimation of carbon dioxide flux degassing from percolating waters in a karst cave:
- 1015 Case study from Bijambare cave, Bosnia and Herzegovina. Geochemistry, 75(4), 465-474.
- 1016 https://doi.org/10.1016/j.chemer.2015.10.004
- 1017
- 1018 Mook, W. G., Bommerson, J. C., & Staverman, W. H. (1974). Carbon isotope fractionation between dissolved bicarbonate
- 1019 and gaseous carbon dioxide. Earth and Planetary Science Letters, 22(2), 169–176.
- 1020 https://doi.org/10.1016/0012-821X(74)90078-8
- 1021
- 1022 Moyes, A. B., Gaines, S. J., Siegwolf, R. T. W., & Bowling, D. R. (2010). Diffusive fractionation complicates isotopic
- 1023 partitioning of autotrophic and heterotrophic sources of soil respiration. Plant, Cell and Environment, 33(11), 1804–1819.
- 1024 Scopus. https://doi.org/10.1111/j.1365-3040.2010.02185.x
- 1025
- 1026 Muhr, J., Borken, W., & Matzner, E. (2009). Effects of soil frost on soil respiration and its radiocarbon signature in a Norway
- 1027 spruce forest soil. Global Change Biology, 15(4), 782–793. https://doi.org/10.1111/j.1365-2486.2008.01695.x
- 1028
- 1029 Nakano, A., Takahashi, K., & Kimura, M. (1999). The carbon origin of arbuscular mycorrhizal fungi estimated from δ13C
- 1030 values of individual spores. Mycorrhiza, 9(1), 41–47. https://doi.org/10.1007/s005720050261
- 1031
- 1032 Noronha, A. L., Johnson, K. R., Southon, J. R., Hu, C., Ruan, J., & McCabe-Glynn, S. (2015). Radiocarbon evidence for
- 1033 decomposition of aged organic matter in the vadose zone as the main source of speleothem carbon. Quaternary Science
- 1034 Reviews, 127, 37–47. https://doi.org/10.1016/j.quascirev.2015.05.021
- 1035
- 1036 Pataki, D. E., Ehleringer, J. R., Flanagan, L. B., Yakir, D., Bowling, D. R., Still, C. J., Buchmann, N., Kaplan, J. O., & Berry,
- 1037 J. A. (2003). The application and interpretation of Keeling plots in terrestrial carbon cycle research. Global Biogeochemical
- 1038 Cycles, 17(1). https://doi.org/10.1029/2001GB001850
- 1039

- 1040 Perrin, J., Jeannin, P.-Y., & Zwahlen, F. (2003). Epikarst storage in a karst aquifer: A conceptual model based on isotopic
- 1041 data, Milandre test site, Switzerland. Journal of Hydrology, 279(1), 106–124.
- 1042 https://doi.org/10.1016/S0022-1694(03)00171-9

- 1044 Planavsky, N., Partin, C., & Bekker, A. (2015). Carbon Isotopes as a Geochemical Tracer. Encyclopedia of Astrobiology,
- **1045** (pp. 366–371). https://doi.org/10.1007/978-3-662-44185-5 228

1046

- 1047 Powers, H. H., Hunt, J. E., Hanson, D. T., & McDowell, N. G. (2010). A dynamic soil chamber system coupled with a
- 1048 tunable diode laser for online measurements of δ 13C, δ 18O, and efflux rate of soil-respired CO2. Rapid Communications in
- 1049 Mass Spectrometry, 24(3), 243–253. https://doi.org/10.1002/rcm.4380

1050

- 1051 Pumpanen, J., Ilvesniemi, H., Perämäki, M., & Hari, P. (2003). Seasonal patterns of soil CO2 efflux and soil air CO2
- 1052 concentration in a Scots pine forest: Comparison of two chamber techniques. Global Change Biology, 9(3), 371-382.
- 1053 https://doi.org/10.1046/j.1365-2486.2003.00588.x

1054

- 1055 Ravn, N. R., Michelsen, A., & Reboleira, A. S. P. S. (2020). Decomposition of Organic Matter in Caves. Frontiers in
- **1056** *Ecology and Evolution*, 8. https://doi.org/10.3389/fevo.2020.554651

1057

- 1058 Reimer, P., Brown, T., & Reimer, R. (2004). Discussion: Reporting and Calibration of Post-Bomb 14C Data. Radiocarbon,
- 1059 46, 1299-1304. https://doi.org/10.1017/S0033822200033154

1060

- 1061 Risk, D., Nickerson, N., Phillips, C. L., Kellman, L., & Moroni, M. (2012). Drought alters respired δ13CO2 from
- 1062 autotrophic, but not heterotrophic soil respiration. Soil Biology and Biochemistry, 50, 26–32.
- 1063 https://doi.org/10.1016/j.soilbio.2012.01.025

1064

1065

- 1066 Sánchez-Cañete, E. P., Barron-Gafford, G. A., & Chorover, J. (2018). A considerable fraction of soil-respired CO2 is not
- 1067 emitted directly to the atmosphere. Scientific Reports, 8(1), 13518. https://doi.org/10.1038/s41598-018-29803-x

1068

- 1069 Savoy, L., Surbeck, H., & Hunkeler, D. (2011). Radon and CO2 as natural tracers to investigate the recharge dynamics of
- 1070 karst aquifers. Journal of Hydrology, 406(3), 148–157. https://doi.org/10.1016/j.jhydrol.2011.05.031

- 1072 Schoell, M. (1980). The hydrogen and carbon isotopic composition of methane from natural gases of various origins.
- 1073 Geochimica et Cosmochimica Acta, 44(5), 649–661. https://doi.org/10.1016/0016-7037(80)90155-6

- 1075 Shi, Z., Allison, S. D., He, Y., Levine, P. A., Hoyt, A. M., Beem-Miller, J., Zhu, Q., Wieder, W. R., Trumbore, S., &
- 1076 Randerson, J. T. (2020). The age distribution of global soil carbon inferred from radiocarbon measurements. Nature
- 1077 Geoscience, 13(8), 555–559. https://doi.org/10.1038/s41561-020-0596-z

- 1079 Sommaruga, A. (2011). From the central Jura mountains to the molasse basin (France and Switzerland). Swiss Bulletin Fuer
- **1080** *Angewandte Geologie*, *16*(2), 63–75.

1081

- 1082 Staddon, P. (2004). Carbon isotopes in functional soil ecology. Trends in Ecology & Evolution, 19, 148-154.
- 1083 https://doi.org/10.1016/j.tree.2003.12.003

1084

- 1085 Stewart, B., Zhi, W., Sadayappan, K., Sterle, G., Harpold, A., & Li, L. (2022). Soil CO2 Controls Short-Term Variation but
- 1086 Climate Regulates Long-Term Mean of Riverine Inorganic Carbon. Global Biogeochemical Cycles, 36(8), e2022GB007351.
- 1087 https://doi.org/10.1029/2022GB007351

1088

- 1089 Stickler, W., Trimborn, P., Maloszewski, P., Rank, D., Papesch, W., Reichert, B. (1997). Environmental Isotope
- **1090** Investigations. Acata Carsologica, 26/1, 236 259.

1091

- 1092 Suess, E., & Whiticar, M. J. (1989). Methane-derived CO2 in pore fluids expelled from the Oregon subduction zone.
- 1093 Palaeogeography, Palaeoclimatology, Palaeoecology, 71(1), 119–136. https://doi.org/10.1016/0031-0182(89)90033-3

1094

1095 Swisstopo. Retrieved 1 December 2024, from https://www.swisstopo.admin.ch/en

1096

- 1097 Synal, H.-A., Stocker, M., & Suter, M. (2007). MICADAS: A new compact radiocarbon AMS system. Nuclear Instruments
- 1098 and Methods in Physics Research Section B: Beam Interactions with Materials and Atoms, 259(1), 7-13.
- 1099 https://doi.org/10.1016/j.nimb.2007.01.138

1100

- 1101 Szidat, S. (2020). ¹⁴C Research at the Laboratory for the Analysis of Radiocarbon with AMS (LARA), University of Bern.
- 1102 CHIMIA, 74(12), Article 12. https://doi.org/10.2533/chimia.2020.1010

1103

- 1104 Treseder, K. K., & Allen, M. F. (2000). Mycorrhizal fungi have a potential role in soil carbon storage under elevated CO2
- 1105 and nitrogen deposition. New Phytologist, 147(1), 189–200. https://doi.org/10.1046/j.1469-8137.2000.00690.x

- 1107 Tomczyk-Żak, K., & Zielenkiewicz, U. (2016). Microbial Diversity in Caves. Geomicrobiology Journal, 33(1), 20-38.
- 1108 https://doi.org/10.1080/01490451.2014.1003341
- 1109
- 1110 Trumbore, S. (2000). Age of Soil Organic Matter and Soil Respiration: Radiocarbon Constraints on Belowground C
- 1111 Dynamics. Ecological Applications, 10(2), 399–411.
- 1112 https://doi.org/10.1890/1051-0761(2000)010[0399:AOSOMA]2.0.CO;2
- 1113
- 1114 Tune, A., Druhan, J., Wang, J., Bennett, P., & Rempe, D. (2020). Carbon Dioxide Production in Bedrock Beneath Soils
- 1115 Substantially Contributes to Forest Carbon Cycling. Journal of Geophysical Research: Biogeosciences, 125.
- 1116 https://doi.org/10.1029/2020JG005795
- 1117
- 1118 Unger, S., Máguas, C., Pereira, J. S., Aires, L. M., David, T. S., & Werner, C. (2010). Disentangling drought-induced
- 1119 variation in ecosystem and soil respiration using stable carbon isotopes. *Oecologia*, 163(4), 1043–1057.
- 1120 https://doi.org/10.1007/s00442-010-1576-6
- 1121
- 1122 Vadillo, I., Ojeda, L., Benavente, J., Liñán, C., Carrasco, F., del Padial, R. (2016). Datación del CO2 mediante 14C del aire
- 1123 de la zona no saturada en la parcela experimental de la Cueva de Nerja (Andalucía, Málaga). En: Andreo, B. y Durán, J.J.
- 1124 (Eds). El karst y el hombre: las cuevas como Patrimonio Mundial. Asociación Cuevas Turísticas Españolas, 327–334.
- 1125
- 1126 Van Rossum, G. & Drake, F.L., 2009. Python 3 Reference Manual, Scotts Valley, CA: CreateSpace.
- 1127
- 1128 Vaughn, L. J. S., & Torn, M. S. (2018). Radiocarbon measurements of ecosystem respiration and soil pore-space CO₂ in
- 1129 Utqiagvik (Barrow), Alaska. Earth System Science Data, 10(4), 1943–1957. https://doi.org/10.5194/essd-10-1943-2018
- 1130
- 1131 Vuilleumier, C., Jeannin, P.-Y., Hessenauer, M., & Perrochet, P. (2021). Hydraulics and turbidity generation in the Milandre
- 1132 Cave (Switzerland). Water Resources Research, 57. https://doi.org/10.1029/2020WR029550
- 1133
- 1134 Wacker, L., Christl, M., & Synal, H.-A. (2010b). Bats: A new tool for AMS data reduction. *Nuclear Instruments and*
- 1135 Methods in Physics Research Section B: Beam Interactions with Materials and Atoms, 268(7), 976–979.
- 1136 https://doi.org/10.1016/j.nimb.2009.10.078
- 1137
- 1138 Wacker, L., Němec, M., & Bourquin, J. (2010a). A revolutionary graphitisation system: Fully automated, compact and
- 1139 simple. Nuclear Instruments and Methods in Physics Research Section B: Beam Interactions with Materials and Atoms,
- 1140 268(7), 931–934. https://doi.org/10.1016/j.nimb.2009.10.067

- 1141
- 1142 Wan, J., Tokunaga, T. K., Dong, W., Williams, K. H., Kim, Y., Conrad, M. E., Bill, M., Riley, W. J., & Hubbard, S. S. (2018).
- 1143 Deep Unsaturated Zone Contributions to Carbon Cycling in Semiarid Environments. Journal of Geophysical Research:
- 1144 Biogeosciences, 123(9), 3045–3054. https://doi.org/10.1029/2018JG004669
- 1145
- 1146 Webster, K.D. et al. (2022) 'Diversity and Composition of Methanotroph Communities in Caves', Microbiology Spectrum,
- 1147 10(4), pp. e01566-21. Available at: https://doi.org/10.1128/spectrum.01566-21.
- 1148
- 1149 Wiseschart, A., Mhuanthong, W., Thongkam, P., Tangphatsornruang, S., Chantasingh, D., & Pootanakit, K. (2018). Bacterial
- 1150 Diversity and Phylogenetic Analysis of Type II Polyketide Synthase Gene from Manao-Pee Cave, Thailand.
- 1151 Geomicrobiology Journal, 35, 518-527. https://doi.org/10.1080/01490451.2017.1411993
- 1152
- 1153 Weissert, H., & Mohr, H. (1996). Late Jurassic climate and its impact on carbon cycling. Palaeogeography,
- 1154 Palaeoclimatology, Palaeoecology, 122(1), 27–43. https://doi.org/10.1016/0031-0182(95)00088-7
- 1155
- 1156 Wingler, A., & Hennessy, D. (2016). Limitation of Grassland Productivity by Low Temperature and Seasonality of Growth.
- **1157** Frontiers in Plant Science, 7. https://doi.org/10.3389/fpls.2016.01130
- 1158
- 1159 Wu, J., Zhang, Q., Yang, F., lei, Y., Zhang, Q., & Cheng, X. (2017). Does short-term litter input manipulation affect soil
- 1160 respiration and its carbon-isotopic signature in a coniferous forest ecosystem of central China? Applied Soil Ecology, 113,
- **1161** 45–53. https://doi.org/10.1016/j.apsoil.2017.01.013
- 1162
- 1163 Zhang, H., Zhou, Z., Dong, H., Yan, L., Ding, S., Huang, J., Gong, X., & Su, D. (2023). Seasonal variations of cave
- 1164 dripwater hydrogeochemical parameters and δ 13CDIC in the subtropical monsoon region and links to regional hydroclimate.
- 1165 Science of The Total Environment, 881, 163509. https://doi.org/10.1016/j.scitotenv.2023.163509
- 1166
- 1167 Zhou, J., Gu, Y., Zou, C., Mo, M. (2007). Phylogenetic diversity of bacteria in an earth-cave in Guizhou province, southwest
- 1168 of China. The Journal of Microbiology, 45(2).
- 1169
- 1170 Zhu, Y.-G., & Miller, R. M. (2003). Carbon cycling by arbuscular mycorrhizal fungi in soil-plant systems. *Trends in Plant*
- 1171 Science, 8(9), 407–409. https://doi.org/10.1016/S1360-1385(03)00184 5